A Combined High-Order Spectral and Boundary Integral Equation Method for Modelling Wave Interactions With Submerged Bodies

by

Gregory Robert Thomas

Submitted to the Department of Ocean Engineering
in partial fulfillment of the requirements for the degree of

Doctor of Philosophy in Hydrodynamics

at the

MASSACHUSETTS INSTITUTE OF TECHNOLOGY

February 1997

Author ..... G. R. Thomas .....
Department of Ocean Engineering
November 4, 1996

Certified by ..... Jerome H. Milgram .....
Jerome Milgram
Professor of Ocean Engineering
Thesis Supervisor

Accepted by ..... J. Kim Vandiver .....
J. Kim Vandiver
Chairman, Departmental Committee on Graduate Students

A Combined High-Order Spectral and Boundary Integral Equation Method for Modelling Wave Interactions With Submerged Bodies

by

Gregory Robert Thomas

Submitted to the Department of Ocean Engineering
on November 4, 1996, in partial fulfillment of the
requirements for the degree of
Doctor of Philosophy in Hydrodynamics

Abstract

The interaction of submerged manuevering vehicles with the free surface is a topic of importance in ocean engineering. Present methods for estimating the forces and motions due to wave-body interactions are limited in their ability to efficiently compute forces and motions of interest when free surface slopes are steep or body motions are large. Methods are required which contribute to overcoming these difficulties.

This thesis presents a method for analyzing the nonlinear interaction of non-breaking waves with submerged bodies of arbitrary geometries undergoing arbitrary motions. The method couples a high order spectral representation of the free surface profile and free surface potential with a boundary element representation of the body to effect a time domain solution for specified initial-boundary value problems. The spectral representation of free surface quantities facilitates the use of fast transform techniques for rapidly computing free surface quantities. The boundary element repesentation of the body enables bodies of arbitrary geometry to be modelled. Fully nonlinear free surface boundary conditions are used as time evolution equations for the free surface profile and potential.

The effectiveness of the method is demonstrated through the solution of three classes of two-dimensional problems: (1) diffraction of incident waves by a stationary cylinder, (2) wave radiation by a cylinder undergoing forced oscillations, and (3) combined diffraction and radiation by a submerged neutrally buoyant cylinder free to respond to incident waves.

Thesis Supervisor: Jerome Milgram
Title: Professor of Ocean Engineering

Acknowledgments

The support of the following are gratefully acknowledged:
The United States Navy for the opportunity to pursue this work.
Captain Al Brown, LCDR Mark Welsh, and LCDR Jeff Reed for their leadership, encouragement and friendship.
Professor Jerome Milgram, my thesis advisor, for his steadfast support, enthusiasm, and guidance.
The members of my thesis committee, Professor T. Francis Ogilvie, Professor J. Nick Newman, and
Dr. F. Thomas Korsmeyer, for their guidance and patience.
Tom Korsmeyer, for good coffee and wise counsel.
Captain Jack McNamee, CDR Mark Lusted, CDR Tom Moore, and LCDR Steve Markle for setting high standards for performance and friendship.
The folks in the lab, past and present- Dr. Fernando Frimm, Dr. Hasan St. Olmez, Dr. Bill Ramsey, Noah Eckhouse, John Mass, Bill Milewski, Soren Jensen, and Nicole Suoja, for putting up with me and pulling me through some difficult times.
The MIT Rugby Team and extended family, in particular, Dr. Leo Casey, Ben Paul, Chevy, John O'Sullivan, Dr. Marthinius van Schoor, Stephan Pretorius, Steve Wilhelm, and Jonathon Kutchins.
Professor A.D. Carmichael for his cheerful support and insight.
Professor Chryssostomidis and the Ocean Engineering Department Staff for making things run smoothly. Dr. Yuming Liu for discussions on the spectral method.
My parents and my brothers, for years of encouragement and support.
My mother and father in-law for helping care for my family.
The staff at Newport Naval Hospital.
Dr. Yuming Liu for discussions on the spectral method.
Most importantly, Mary, Sarah, Matthew, and Michael, for their support and love. They cheerfully sacrificed a great deal and were a source of light and hope. I am forever in their debt.

Contents

List of Figures

List of Tables

Chapter 1

Introduction and Background

This thesis presents a method for solving wave body interaction problems. The method developed is appropriate to the analysis of the nonlinear interaction of non-breaking waves with fully submerged bodies of arbitrary geometry undergoing arbitrary motions. The method is suitable for the study of three or two dimensional problems. The efficacy of the method is demonstrated through the study of three classes of two dimensional problems:

- The diffraction of an incident Stokes' wave by a fully submerged cylinder of arbitrary shape;
- The wave radiation by a fully submerged circular cylinder undergoing large amplitude forced oscillatory motion; and,
- The response of a neutrally buoyant circular cylinder to an incident Stokes' wave (combined radiation and diffraction).

The purpose of this chapter is to explain the motivation, background, and format for this thesis.

1.1 Motivation

This thesis is motivated by the desire to efficiently estimate and understand the interaction of fully submerged bodies with the free surface. A time domain solution for the forces resulting from the interaction of the body with waves is necessary to perform maneuvering simulations of bodies operating near the free surface. Present methods for estimating forces due to wave-body interactions limit the computing speed of maneuvering simulation calculations or include linearizing assumptions which limit the ability to predict forces and motions of interest when free surface slopes are steep or unsteady body motions are large. This thesis presents a method which overcomes some of these shortcomings.

1.2 Background

The Physical Problem

The complete physical problem for a body operating in proximity to a free surface is dominated by inertial, viscous, and gravitational forces [33]. Other mechanisms, such as surface tension, exist but are insignificant. A mathematical representation of the complete physical problem amenable to efficient solution does not exist. The problem includes the possibility of separated flows and breaking waves, phenomena difficult to analyze. Numerical methods enable a range of problems that include some of these phenomema to be solved, however the computing time required by some methods to solve these problems for arbitrary bodies is prohibitively excessive. For example, the solution of the Navier-Stokes equations for the flow around a submarine in an unbounded fluid for six body lengths of travel requires as much as 100 hours of CPU time on an IBM Model 590 workstation with 512 MB of RAM [27]. Numerical methods are needed which can characterize the relevant fluid and body

behavior with improved computational efficiency.

The relative importance of the principal force mechanisms varies as the parameters characterizing the problem change. Dimensional analysis is used to define the relationships between the force mechanisms and identify ranges of problem parameters over which one or more of the force mechanisms may be ignored. For a typical marine vessel moving beneath the free surface the ratio of inertial to viscous forces is large outside the boundary layer. The fluid can be treated as inviscid and the governing mathematical representation of the problem appropriately simplified [33]. If the problem is further restricted to considering only non-breaking waves, a wide range of practical problems can be solved. In the following section, the existing methods for solving wave-body interaction problems for inviscid fluids under non-breaking waves are briefly discussed.

Solution Methods

The simplest solution method is that proposed by Faltinsen [9]. This method approximates the hydrodynamic force as the sum of (1) the Froude-Krylov Force (F_{FK}), the force due to the unsteady pressure field associated with the undisturbed incident wave potential; (2) a force proportional to the product of the body's added mass and the acceleration vector of the undisturbed wave field; and (3) the added mass force, the force resulting from the body's acceleration. This approach has been used [5] for simulating the forces associated with undersea vehicles operating near the free surface. The shortcomings of this type of approach are discussed by Newman [32] and Milgram [29]. This approach can only be accurate if

- The Froude Numbers based on submergence depth, F_H, and body length, F_L are small:

$$F_H = \frac{V_s}{\sqrt{gH}} \ll 1 \quad \text{and} \quad F_L = \frac{V_s}{\sqrt{gL}} \ll 1 \tag{1.1}$$

where V_s is the body velocity, g is the gravitational constant, H is the body's mean submergence, and L is the body's length; and,

- The body is small compared to the wavelength.

Because of these restrictions, the method is not suitable for many combinations of marine vessels and operating scenarios of interest.

Numerical solution methods for wave-body interaction problems exist in both the frequency and time domains. The application of the principle of linear superposition to ship motions in irregular seas was motivated by the work of John [15] and St. Denis and Pierson [44]. The former, as noted by Korsmeyer [19], enabled the problem to be decomposed into separate radiation and diffraction problems, and the latter, as noted by Salvesen, et al. [40], enabled ship responses in irrregular seas to be evaluated as the sum of the responses at all frequencies of regular waves. Jointly these works motivated the development of a wide body of linearized ship motion analysis methods in the frequency domain using strip theory and slender body theory to characterize the wave-body interaction. The work of Salvesen, Tuck, and Faltinsen [40] is a thorough application of strip theory to ship motion analysis. Ogilvie [36] provides a thorough development of slender body theory and its application to ship motions.

Improvements in digital processing capabilities enabled the development of three dimensional analysis methods for arbitrary wave induced ship motions [2]. Solution methods have evolved systematically, from the solution to the linearized problem for stationary bodies or bodies undergoing forced motion to the solution for bodies undergoing nonlinear unsteady

motions with forward speed. Both frequency and time domain solution methods have developed for such problems. The solution to the specified boundary value or initial value problems is found by either volume methods (finite difference and finite element methods) or boundary integral equation methods (boundary element or "panel" methods) [7]. The present preferred methods in ship hydrodynamics are the boundary integral equation methods (BIEM). Kring [20] summarizes the development of three dimensional panel methods, with emphasis in his summary on the distinction between methods which use the transient free surface Green function (Korsmeyer [19] and Bingham [2]) and those which use the Rankine source (Nakos [31] and Kring [20]). Time domain simulations of wave-induced motions are of immediate interest for their applicability to vehicle motion control and control system design.

Dommermuth [7] and Liu [22] developed a high-order spectral method (HOSM) for the efficient time-domain analysis of non-linear wave-body interactions. The high-order spectral method, through the use of Fast Fourier Transform (FFT) techniques, greatly improves the computational efficiency of the numerical analysis of wave-body interactions.

The solution method developed in this thesis couples the boundary integral representation of the body with a spectral representation of free surface quantities. To demonstrate the efficacy of the method, the three classes of problem identifed previously, radiation, diffraction, and combined radiation and diffraction, are studied for two dimensional bodies. The solutions are compared with solutions generated by different methods for similar two dimensional problems. These other methods will be briefly summarized here. A similar summary of some of these methods and related methods can be found in Dommermuth [7] and Liu [22]. More detailed discussions of the methods and the solutions generated will be discussed in subsequent chapters as appropriate.

Frequency domain solutions to wave diffraction and radiation by circular cylinders were developed by Ursell [47] and Ogilvie [35]. Ursell used a multipole expansion of the pulsating source potential and a series expansion, in powers of the wave slope, for the coefficients in the multipole expansion, to derive a system of equations to uniquely determine the linear solution to the interaction between waves and a fully submerged stationary circular cylinder. Ogilvie extended Ursell's work to compute the first-order unsteady force and the second-order steady force for the three problems of interest in this thesis. Wu [53] extended Ogilvie's work using the multipole expansion and the free surface boundary condition for the second order potential to demonstrate that to second order, a circular cylinder undergoing a circular orbit generates waves in one direction only. Ogilvie previously demonstrated this result at first order. Using a linear free surface boundary condition and the exact body boundary condition, Wu [52] found that a circular cylinder undergoing large-amplitude circular motion can generate waves travelling in both directions though the waves travelling in the "upstream" direction were at most a third order quantity.

Chapman [4] analyzed large amplitude transient motions of two-dimensional bodies with a linearized free surface boundary condition and exact body boundary conditions. Chapman represented the wave field as a finite sum of eigenfunctions and the body as a distribution of sources and negative image sources reflected about the mean free surface. For Chapman's method the periodic boundary conditions required by the spectral representation of free surface quantities are ignored in the representation of the body potential, the harmonic components used to represent the free surface quantities are nonuniform and can not be determined by FFT, and the method is applicable to flows described by linear free surface boundary conditions.

Grue and Palm [11] studied the reflection of waves by submerged cylinders of circular and elliptic cross section using boundary integral equations. In their formulation the solution is expressed as a distribution of vortices on the body. Grue and Palm used the linear free surface boundary conditions in their formulation and confirmed the results of Ursell and Ogilvie (no reflection from a circular cylinder) and computed the reflection power for the elliptic contour. Their analyses of cylinders of elliptic cross section are restricted to deeply submerged cylinders.

Stansby and Slaouti [45] developed a time domain solution method for evaluating non-linear wave-body interactions with the free surface represented as a periodic vortex sheet and the body as a distribution of periodic sources. The focus of their work was on the first order oscillatory forces and wave motions only and they demonstrated reasonable agreement with the first order solution of Ogilvie, in both the amplitude and phase of the oscillatory forces.

A numerical solution to the second-order wave diffraction problem in the frequency domain was provided by Vada [48]. Vada derived the boundary conditions for the first and second order diffraction potentials using perturbation expansions of the boundary conditions and solved the first and second order problems using a boundary element method. Vada used the frequency domain free surface Green function provided by Wehausen and Laitone [50] for the first order problem and a suitable modification of it for the second order problem. The results generated by this method compare favorably with the results of Ogilvie and experimental results [3]. Vada did not solve for the time-independent part of the second order potential and restricted his study to stationary bodies.

The Mixed Eulerian-Lagrangian (MEL) method has been applied to the study of non-linear wave body interactions by a number of authors. Vinje and Brevig [49] and Cointe [6]

studied the interaction of cylinders with non-linear free surface boundary conditions. Vinje and Brevig demonstrated the suitability of the approach to the study of wave-body interactions. Cointe studied the diffraction and radiation problems in detail and demonstrated the ability of non-linear solution methods to capture behavior not predicted by linear and second order theories. However, the Lagrangian representation of free surface quantities is not amenable to solution by fast transform techniques.

Vinje and Brevig's work, which used Cauchy's integral theorem to represent the velocity potential and stream function , was used by Jagannathan [14] to study radiation conditions for the MEL method. In the process, Jagannathan produced time simulations for the forces on a submerged circular cylinder. The force results vary significantly from theortical and experimental results for wave diffraction but show better agreement for forced motions. Additionally, the difference between Jagannathan's results and experimental results increases as submergence decreases.

Silva and Peregrine [43] also used the MEL approach to study nonlinear wave-body interaction problems for submerged fixed bodies and submerged bodies undergoing forced oscillatory motions. Silva and Peregrine demonstrated the influence of finite depth on the forces and free surface profiles associated with forced body motion. Silva and Peregrine's approach is not extendable to three dimensions.

The high-order spectral methods (HOSM) of Dommermuth and Liu have been used to study nonlinear wave-body interactions in both three and two dimensions. By performing computations at orders higher than second order, Dommermuth and Liu were able to compute a steady horizontal drift force acting on a fixed submerged circular cylinder. This force is not predicted by second order theories but has been measured experimentally [30] and computed by fully nonlinear methods [6]. The HOSM uses the FFT to rapidly compute the

body and free surface potential. The HOSM requires that the body be capable of being efficiently represented by series of orthogonal functions. Additionally, the HOSM represents the body potential as a Taylor series expansion about the mean body position. Therefore, the method can not be used to model a body undergoing large amplitude unsteady motions.

1.3 Thesis Format

This thesis consists of seven chapters. The mathematical formulation of the combined high-order spectral boundary integral equation method is provided as Chapter 2. The numerical implementation of the method is provided in Chapter 3. The results for the radiation, diffraction, and combined problems are provided in Chapters 4, 5, and 6 respectively. Chapter 7 provides conclusions and recommendations for future work.

Chapter 2

Approach

This chapter presents the method developed for evaluating the interaction of a fully submerged body with the free surface. The problem statement, the solution formulation, and issues associated with the formulation are presented.

2.1 Introduction

The motivation for the mathematical formulation to follow is the solution of the equation of motion for a submerged body subject to both deterministic and stochastic forcing. The deterministic forcing is the result of control surface motions and operation of propulsive devices. The stochastic forcing is due to the interaction of the body and its appendages with waves. The problem formulation presented here provides an efficient method for computing the forces and moments on a fully submerged body of arbitrary geometry due to its interaction with waves.

The formulation provides a mathematical model for the physical problem represented by Figure 2-1.

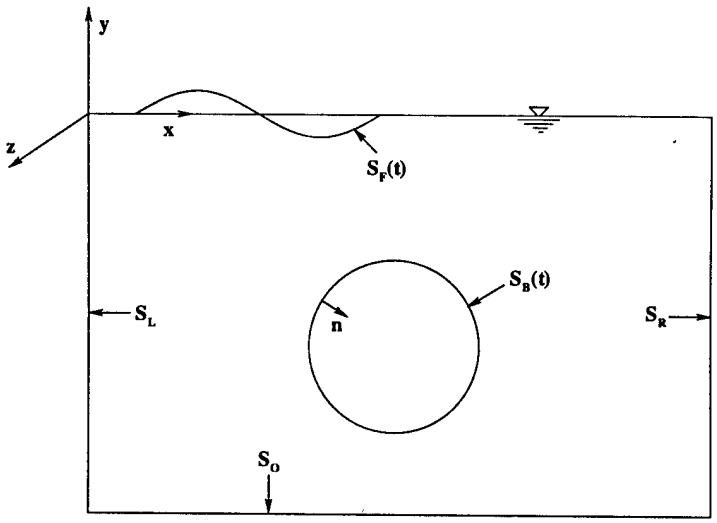

Figure 2-1: Coordinate system definition

2.2 The Initial-Boundary Value Problem

Field Equation

For a large portion of the range of Froude numbers and Reynold's numbers at which marine vessels operate while in proximity to the free surface, viscous effects are confined to a thin layer of fluid near the vessels' surfaces. Prandtl's boundary layer theory motivates and provides justification for neglecting viscous effects in the study of selected problems in hydrodynamics [33]. Chaplin [3] demonstrated experimentally that in the absence of viscous fluid effects significant non-linear wave forces exist.

Wave-body interactions are dominated by fluid flows which can idealized as inviscid and irrotational. Therefore a portion of the non-linear aspects of wave-body interactions can be studied using potential flow theory.

For an incompressible fluid of constant density the equation for conservation of mass is the continuity equation

$$\nabla \cdot \mathrm{V} = 0 \tag{2.1}$$

For an ideal fluid initially at rest and subject to conservative forces the fluid rotation rate is zero and

$$\nabla \times \mathrm{V} = 0 \tag{2.2}$$

The velocity vector for an ideal irrotational flow can be defined as the gradient of a scalar potential

$$\mathrm{V} = \nabla \Phi \tag{2.3}$$

Equations (2.1) and (2.3) are combined to yield Laplace's equation, the governing partial differential equation for the velocity potential:

$$\nabla^2 \Phi = 0 \tag{2.4}$$

Boundary Conditions

The following boundary conditions are imposed on the physical problem represented by Figure 2-1:

$$\frac{\partial \Phi}{\partial n} = 0 \qquad \text{on } S_O \tag{2.5}$$

$$\frac{\partial \Phi}{\partial n} = \vec{U} \cdot \hat{n} \qquad \text{on } S_B(t) \tag{2.6}$$

$$\Phi \mid_{x=0} = \Phi \mid_{x=2L} \tag{2.7}$$

$$\nabla\Phi \mid_{x=0} = \nabla\Phi \mid_{x=2L} \tag{2.8}$$

$$\frac{D}{Dt}(y - \eta) = 0 \qquad \text{on } y = \eta \tag{2.9}$$

$$-\frac{1}{\rho}(p - p_a) = \frac{\partial \phi}{\partial t} + \frac{1}{2}\nabla\phi \cdot \nabla\phi + gy = 0 \qquad \text{on } y = \eta \tag{2.10}$$

where $\eta(x, z, t)$ is the shape of the free surface, $\vec{U}$ is the body velocity, and $2L$ is the domain length.

In the absence of a bottom:

$$\nabla\Phi \rightarrow 0 \qquad \text{as y} \rightarrow -\infty \tag{2.11}$$

The specified form of the kinematic and dynamic free surface boundary conditions (equations (2.9) and (2.10) respectively) determines the type of free surface flows represented. An Eulerian form of the free surface boundary conditions capable of describing non-linear single-valued free surface flows is used in this thesis. The chosen form was developed by Zakharov [55] for the purpose of evaluating the stability of dispersive surface waves. The

"Zakharov Equations" express the free surface boundary conditions as functions of the canonical variables $\Phi^S(x,z,t) \equiv \Phi(x,\eta,z,t)$ and η, and the vertical velocity on the free surface, $\Phi_y(x,\eta,z,t)$:

$$\eta_t = (1+\eta_x^2)\Phi_y(x,\eta,t) + \Phi_x^S\eta_x \tag{2.12}$$

$$\Phi_t^S = -g\eta - \frac{1}{2}(\Phi_x^S)^2 + \frac{1}{2}(1+\eta_x^2)\Phi_y^2(x,\eta,t) \tag{2.13}$$

Spatial periodicity (equations (2.7) and (2.8)) is specified. The significance of this condition is explained in chapter 3.

Initial Conditions

The initial conditions for the the shape of the free surface, $\eta(x,z,0)$, and the free surface potential, $\Phi^S(x,z,0)$, are specified as those associated with Stokes' waves.

2.3 Solution Method

The Zakharov forms of the kinematic and dynamic free surface boundary conditions are integrated in time to update the free surface shape and free surface potential using the specified initial conditions and the solution of the boundary value problem. A combined high-order spectral method (HOSM) and boundary integral equation method (BIEM) is used to solve the specified initial-boundary-value problem. The Zakharov equations were used in the HOSM developed by Dommermuth and Yue [8] and West, et. al. [51] to solve non-linear wave-wave interaction problems and by Liu, Dommermuth, and Yue [23] to evaluate non-linear wave-body interactions. Olmez [37] used the Zakharov equations and

a boundary integral equation method to analyze non-linear wave-wave interaction problems.

The high order spectral method (HOSM) and (BIEM) are summarized in the following sections.

High-Order Spectral Method

The HOSM summarized here is that of Liu, Dommermuth, and Yue [23] for solving nonlinear wave-body interaction problems. In the HOSM, and in the combined HOSM-BIEM solution method developed herein, the velocity potential is expanded in a perturbation series up to a specified order M:

$$\Phi^{(m)}(x,y,z,t) = \sum_{m=1}^{M} \Phi^{(m)}(x,y,z,t) \tag{2.14}$$

$(\ )^{(m)}$ denotes a quantity of order $(\epsilon)^{(m)}$ where ϵ is a measure of wave steepness, kA.

Each perturbation potential, $\Phi^{(m)}(x,y,z,t)$, is expanded in a Taylor series about $y = 0$ such that:

$$\Phi^{S}(x,z,t) \equiv \Phi(x,\eta,z,t) = \sum_{m=1}^{M} \sum_{l=0}^{M-m} \frac{\eta^l}{l!} \frac{\partial \eta^l}{\partial y^l} \Phi^{(m)}(x,y,z,t) \tag{2.15}$$

For the specified initial conditions, equation (2.15) establishes a sequence of Dirichlet boundary conditions for each perturbation potential, $\Phi^{(m)}(x,0,z,t)$:

$$\Phi^{(1)}(x,0,z,t) = \Phi^{S}(x,z,t) \tag{2.16}$$

$$\Phi^{(m)}(x,0,z,t) = -\sum_{l=1}^{m-1} \frac{\eta^l}{l!} \frac{\partial^l}{\partial y^l} \Phi^{(m-l)}(x,0,z,t) \ , \qquad m = 2,3,\ldots,M \tag{2.17}$$

The HOSM, as developed for wave-wave interactions, represents the velocity potential at each order as a Fourier series. The amplitude of each Fourier mode is determined, at each order m, by the Dirichlet conditions expressed above. In the HOSM developed for solving wave-body interaction problems, the velocity potential at each order is expressed as the sum of expansions of free surface and body basis functions [23]:

$$\Phi^{(m)}(x,y,z,t) = \sum_{n=0}^{\infty} \mu_n^{(m)}(t) \Psi_{Fn}(x,y,z) + \sum_{n=0}^{\infty} \sigma_n^{(m)}(t) \Psi_{Bn}(x,y,z) \tag{2.18}$$

where $\mu_n(t)$ are the Fourier modal amplitudes of dipoles distributed on the free surface and $\sigma_n(t)$ are the Fourier modal amplitudes of sources distributed on the body.

The basis functions, Ψ_{Fn} and Ψ_{Bn}, satisfy the Laplace equation, spatial periodicity requirements, and the bottom boundary conditions. For two dimensional problems, for example, the basis functions are given as Fourier integrals involving the two-dimensional periodic source potential. A derivation and explanation of the two-dimensional periodic source potential are available in Newman [34].

Boundary Integral Equation Method

A boundary value problem governed by the Laplace equation can be recast as a boundary integral equation for the unknown velocity potential [13]. A review of the boundary integral equation method is available in Hunt [13].

The boundary integral equation method (BIEM) uses Green's theorem to derive an

integral equation for the velocity potential in terms of distributions of singularities on the boundary of a simply connected fluid domain. The velocity potential is expressed as a function of singularity distributions on the fluid boundary by applying the second form of Green's Theorem [12]

$$\int \int_S \left[\phi \frac{\partial G}{\partial n} - G \frac{\partial \phi}{\partial n}\right] dS = 0 \tag{2.19}$$

where the Green function G and the velocity potential Φ are solutions of the Laplace equation in the fluid domain.

If the Green function is the potential of a source ($G = \log r$), equation (2.19) can be replaced by [13],

$$\int \int_{S_B} \phi(\xi) \frac{\partial G(\vec{x}, \xi)}{\partial n(\xi)} \, dS_\xi - \int \int_{S_B} G(\vec{x}, \xi) \frac{\partial \phi(\xi)}{\partial n(\xi)} \, dS_\xi = T\phi(\vec{x}) \tag{2.20}$$

where $T = 0, -2\pi, \text{or} -4\pi$ for points outside, on the boundary, or inside the volume defined by the surface $S = S_B \cup S_O \cup S_L \cup S_R \cup S_F$ of Figure 2-1.

The choice of Green function G is determined by the boundary conditions and the type of flow to be modeled. A complete development of the boundary integral equation method (BIEM) is available in Hunt [13].

The Combined High-order Spectral and Boundary Integral Equation Method

The combined high-order spectral and boundary integral equation method (hereinafter re-

ferred to as the 'combined method') eliminates the limitations of the base methods identified in Chapter 1. In particular, arbitrary body shapes are accommodated and all body boundary conditions are satisfied on the exact positions of moving bodies. The combined method defines a "total potential", $\Phi_T(x,y,z,t)$, as the sum of a "spectral potential", $\Phi_{sp}(x,y,z,t)$, and a "body potential", $\Phi_B(x,y,z,t)$. These potentials are defined by the following relationships:

$$\Phi_T(x,y,z,t) \equiv \sum_{m=1}^{M} \Phi_T^{(m)}(x,y,z,t) \tag{2.21}$$

$$\Phi_{sp}(x,y,z,t) \equiv \sum_{m=1}^{M} \Phi_{sp}^{(m)}(x,y,z,t) \tag{2.22}$$

$$\Phi_B(x,y,z,t) \equiv \sum_{m=1}^{M} \Phi_B^{(m)}(x,y,z,t) \tag{2.23}$$

In the combined method $\Phi_T(x,y,z,t)$ is constructed to satisfy the initial-boundary value problem specified above.

The function representing the body potential is chosen to set the body's contribution to the potential on the mean free surface to zero. For a non-lifting body the potential is that of a periodic array of sources located on the body's surface and its negative image. This choice is motivated by the sequence of boundary conditions used to determine the potential at each order, $\Phi^{(m)}(x,0,z,t)$, (equations 2.16 and 2.17). The sequence of boundary conditions to be satisfied on the mean free surface is

$$\Phi_T^{(1)}(x,0,z,t) = \Phi_{sp}^{(1)}(x,0,z,t) + \Phi_B^{(1)}(x,0,z,t) = \Phi^S(x,0,z,t) \tag{2.24}$$

and

$$\Phi_T^{(m)}(x,0,z,t) = \Phi_{sp}^{(m)}(x,0,z,t) + \Phi_B^{(m)}(x,0,z,t) = -\sum_{l=1}^{m-1} \frac{\eta^l}{l!}\frac{\partial^l}{\partial y^l}\Phi^{(m-l)}(x,0,z,t) \ , \qquad m = 2,3,\ldots,M \tag{2.25}$$

As stated above, the body potential's contribution to the velocity potential on the mean free surface is zero. With this choice the left hand sides of equations (2.24) and (2.25) are conditions to be satisfied by the spectral potential. At each order, the right hand sides are known Dirichlet boundary conditions. The coefficients of the Eigenfunction expansions which represent the spectral potential are determined directly from equations (2.24) and (2.25).

In the combined method the body boundary condition is

$$\frac{\partial \Phi_T}{\partial n} = \frac{\partial \Phi_{sp}}{\partial n} + \frac{\partial \Phi_B}{\partial n} = \vec{U} \cdot \hat{n} \text{ on } S_B(t) \tag{2.26}$$

where $\vec{U}$ is the body velocity and $\hat{n}$ is the body unit normal vector.

In the combined method $-\partial\Phi_{sp}/\partial n|_{S_B}$ is added to the body's normal velocity to yield the condition to be satisfied by the singularity distribution on the body. For a non-lifting body the condition is:

$$\frac{\partial}{\partial n}\left[\int\int_{S_B} \sigma(\xi) G(\vec{x},\xi)\, dS_\xi\right] = -\frac{\partial \Phi_{sp}^{(m)}}{\partial n}|_{S_B} + \vec{U}\cdot\hat{n} \ , \qquad m = 1 \tag{2.27}$$

$$\frac{\partial}{\partial n}\left[\int\int_{S_B} \sigma(\xi) G(\vec{x},\xi)\, dS_\xi\right] = -\frac{\partial \Phi_{sp}^{(m)}}{\partial n}|_{S_B} \ , \qquad m = 2,3,\ldots,M \tag{2.28}$$

where $\sigma(\xi)$ is the function describing the source distribution on the body surface. Equations (2.27 and (2.28) can derived from the second form of Green's theorem [17] or by directly assuming that the body can be represented by a distribution of sources along the body boundary.

The coupling of the body and and spectral potentials occurs through the body boundary condition, equations (2.27) and (2.28), and the free surface boundary conditions, equations (2.12), (2.13), (2.24) and (2.25) . The value of the body potential's contribution to the total potential on the mean free surface is zero; the value of the vertical component of the gradient of the body's potential on $y = 0$, $\partial\Phi_B/\partial y|_{(x,0,z,t)}$ is not. The body contributes to the conditions to be satisfied on $y = 0$ through this quantity.

Force

The force on a body due to the dynamic pressure in an ideal, incompressible, irrotational fluid is obtained by integrating the pressure over the body surface [33]:

$$\mathbf{F} = \int \int_{S_B} p\, \mathbf{n}\, d\mathbf{S} \tag{2.29}$$

$$\mathbf{M} = \int \int_{S_B} p\, (\mathbf{r} \times \mathbf{n})\, d\mathbf{S} \tag{2.30}$$

The useful forms of equations (2.29) and (2.30) are derived by applying to the unsteady form of Bernouilli's equation either (1) the kinematic transport theorem and Gauss' theorem or (2) the definition of the exact differential of the potential. If method (1) is applied the resulting force expression is [33]

$$F = -\rho \frac{d}{dt} \iint_{S_B} \phi\, \mathbf{n}\, dS - \frac{1}{2} \left(\nabla\phi \cdot \nabla\phi\, \mathbf{n}\right)\, dS + \rho \iint_{S_B} \left(\frac{\partial\phi}{\partial n}\right) \nabla\phi\, dS \tag{2.31}$$

The following expression for the force is a result of the application of method (2) ([16] and [54])

$$F = -\rho \frac{d}{dt} \iint_{S_B} \phi \, \mathbf{n} \, dS - \frac{1}{2} \left(\nabla\phi \cdot \nabla\phi \, \mathbf{n} \right) dS + \rho \iint_{S_B} \left(\mathbf{U} \cdot \nabla\phi \right) \mathbf{n} \, dS \qquad (2.32)$$

The force expressions differ in the third term on their respective right hand sides. The difference between the expressions is explored in Chapter 5.

Equation of Motion

The equation of motion for a rigid body is derived from Newton's Laws. The appropriate expression of dynamic equilibrium for a direct simulation of the free and forced motions of a submerged body is Newton's Second Law [20]

$$\mathbf{M} \, \ddot{\vec{\mathrm{X}}}(t) = \vec{\mathrm{F}}(t) \qquad (2.33)$$

M is the body mass matrix, $\ddot{\vec{\mathrm{X}}}(t)$ is the body acceleration vector, and $\vec{\mathrm{F}}(t)$ is the force vector. $\vec{\mathrm{F}}(t)$ includes the wave and control surface forcing. The solution of the equation of motion for a body enables simulation of free and forced motions. The calculation of the wave forcing presently controls motion simulation computation speed and is a principal motivation for this thesis.

A state variable representation of the body kinematics makes direct use of the solution of equation (2.33) to simulate body motions in a time varying flow

$$\delta\dot{\vec{X}}(t) = \int_t^{t+\delta t} \ddot{\vec{X}}(t)\, dt \tag{2.34}$$

$$\delta\vec{X}(t) = \int_t^{t+\delta t} \dot{\vec{X}}(t)\, dt \tag{2.35}$$

Equations (2.34) and (2.35) are used to update the body velocity and position

$$\dot{\vec{X}}(t+\delta t) = \dot{\vec{X}}(t) + \delta\dot{\vec{X}}(t) \tag{2.36}$$

$$\vec{X}(t+\delta t) = \vec{X}(t) + \delta\vec{X}(t) \tag{2.37}$$

In the following section the equations used to implement the combined method in two dimensions are presented.

2.4 Implementation of the Combined Method in Two Dimensions

The combined high-order spectral method - boundary integral equation method formulated for two and three dimensions has been implemented in two dimensions in this thesis. The purpose of this section is to present the equations used to carry out this implementation.

The chosen representation of the body potential enables the initial condition for the free surface potential, $\Phi^S(x, t=0)$, to be used with equation 2.24 to determine the initial coefficients of the eigenfunctions which represent the spectral potential:

$$\Phi_T^{(1)}(x, 0, t=0) = \Phi_{sp}^{(1)}(x, 0, t=0) + \Phi_B^{(1)}(x, 0, t=0) = \Phi^S(x, t=0) \tag{2.38}$$

With the body potential represented as an array of sources and its negative image,

$$\Phi_B^{(1)}(x,0,t) = 0 \tag{2.39}$$

and the value of the spectral potential on the mean free surface is

$$\Phi_{sp}^{(1)}(x,0,t=0) = \Phi^S(x,t=0) \tag{2.40}$$

The spectral potential eigenfunction expansion is represented as a Fourier series and the coefficients of each mode, $\Phi_{n_{sp}}^{(1)}(0)$ are determined by

$$\Phi_{sp}^{(1)}(x,0,t=0) = \sum_{n=1}^{N} \Phi_{n_{sp}}^{(1)}(0)\Psi_n(x,0) \tag{2.41}$$

The representation of the spectral potential is similar to that of the HOSM of Dommermuth and Yue [8].

The initial body velocity, $\vec{U}(0)$, and the gradient of the first order spectral potential, $\nabla\Phi_{sp}^{(1)}(x,y)$, are used with the first order body boundary condition to determine the first order source distribution on the body $\sigma^{(1)}(x,y,t)$:

$$\frac{\partial}{\partial n}\left[\int_{S_B} \sigma^{(1)}(x,y,t=0)G(x,y,x',y')\,dS_B\right] = \vec{U}\cdot\hat{n} - \frac{\partial\Phi_{sp}^{(1)}(x,y)}{\partial n}\,|_{S_B} \tag{2.42}$$

where $G(x,y,x',y')$ is the potential of a periodic array of sources [34] and its negative image reflected about $y=0$

$$\begin{aligned} G(x,y,x',y') &= \frac{1}{2}\log\left(2\cosh\frac{\pi(x-x')}{2L}-2\cos\frac{\pi(y-y')}{2L}\right) \\ &- \frac{1}{2}\log\left(2\cosh\frac{\pi(x-x')}{2L}-2\cos\frac{\pi(y-(2h_o-y'))}{2L}\right) \end{aligned} \tag{2.43}$$

where h_o is the depth of the body's centroid.

The first order source distribution on the body and the first order spectral potential are the forcing for the solution of the second order problem through the boundary condition imposed on $\Phi_T^{(2)}(x,0,t)$:

$$\Phi_T^{(2)}(x,0,t) = \Phi_{sp}^{(2)}(x,0,t) + \Phi_B^{(2)}(x,0,t) \tag{2.44}$$

As with the first order body potential, $\Phi_B^{(2)}(x,0,t) = 0$. Therefore equations (2.44) and equations (2.25) are combined to yield the condition to be satisfied by $\Phi_{sp}^{(2)}(x,0,t)$:

$$\Phi_{sp}^{(2)}(x,0,t) = -\eta\frac{\partial\Phi_{sp}^{(1)}(x,0,t)}{\partial y} - \eta\frac{\partial\Phi_B^{(1)}(x,0,t)}{\partial y} \tag{2.45}$$

The second order spectral potential is used in the body boundary value problem to solve for the second order body potential.

$$\frac{\partial\Phi_B^{(2)}}{\partial n}\,|_{S_B} = -\frac{\partial\Phi_{sp}^{(2)}}{\partial n}\,|_{S_B} \tag{2.46}$$

The sequence used to determine the second order source strengths and the higher order spectral potentials follows that used for the first order quantities above.

With the body and spectral potentials known to the desired order M, the quantities needed to compute the pressure and force on the body are known. For a body free to respond to the waves, the force is computed and used to update the body's state using the methods described above.

The body and spectral potentials are used with the Zakharov equations to update the free surface potential and free surface shape. The quantities needed are

$$\frac{\partial \eta(x,t)}{\partial x}, \quad \frac{\partial \Phi^S(x,t)}{\partial x}, \text{ and } \quad \frac{\partial \Phi_T(x,\eta,t)}{\partial y} \tag{2.47}$$

$\partial\eta(x,t)/\partial x$ and $\partial\Phi^S(x,t)/\partial x$ are calculated in spectral space, by the method used by Dommermuth, Yue, and Liu [23]. $\partial\Phi_T(x,\eta,t)/\partial y$ is calculated by determining the contributions of the body and spectral potentials separately. The spectral potential's contribution is computed as in [23] and [8]:

$$\frac{\partial \Phi_{sp}(x,\eta,t)}{\partial y} = \sum_{m=1}^{M} \sum_{k=0}^{M-m} \frac{\eta^k}{k!} \sum_{n=1}^{N} \Phi_{n_{sp}}^{(m)}(t) \frac{\partial^{k+1}}{\partial y^{k+1}} \Psi_n(x,0) \tag{2.48}$$

The body's contribution at each order to the fluid vertical velocity on the free surface,

$$\frac{\partial \Phi_B^{(m)}(x,\eta,t)}{\partial y} \tag{2.49}$$

can be computed directly on the free surface or by Taylor series expansion of the vertical component of partial derivatives of the body potential evaluated on $y = 0$. For $k \geq 1$, $\partial^k \Phi_B^{(m)} / \partial y^k$ is made computationally efficient using Laplace's equation to reduce the number of y derivatives required [23].

Chapter 3

Numerical Implementation

The initial boundary value problem defined in the previous chapter is solved numerically. The purpose of this chapter is to describe the numerical implementation of the mathematical formulation. This chapter will:

- Present the problem in the form of systems of discretized equations to be solved by appropriate numerical methods;
- Analyze the accuracy, consistency, and stability of the proposed numerical scheme; and
- Demonstrate necessary conditions for the method to converge to solutions of the physical problems of interest.

3.1 System of Equations

The method developed for solving the initial boundary value problem requires the solution of a system of equations at each time step. The system of equations is determined by the specified form of the boundary conditions in the initial boundary value problem. The form

of the free surface boundary conditions, the periodic nature of the problem formulation, and the choice of a boundary integral representation of the body determine the characteristics of the numerical formulation.

The numerical solution is enforced at points along the boundary of the computational domain $S = S_B \cup S_O \cup S_L \cup S_R \cup S_F$ of Figure 2-1. The solution is enforced at N_X evenly spaced points along the horizontal (x) axis, N_B evenly spaced points around the body, and N_O evenly spaced points along the bottom.

The system of equations developed to represent the boundary value problem at each time step is expressed symbolically in matrix form as

$$\begin{bmatrix} [\mathbf{F}] & [\mathbf{L_{BW}}] & [\mathbf{L_{OW}}] \\ \left[\mathbf{F}'_{\mathbf{B}}\right] & [\mathbf{L_{BB}}] & [\mathbf{L_{OB}}] \\ \left[\mathbf{F}'_{\mathbf{O}}\right] & [\mathbf{L_{BO}}] & [\mathbf{L_{OO}}] \end{bmatrix} \begin{bmatrix} \left[\mathbf{\Phi}^{(\mathbf{m})}_{\mathbf{sp}}\right] \\ \mathbf{\Phi}^{(\mathbf{m})}_{\mathbf{B}} \\ \mathbf{\Phi}^{(\mathbf{m})}_{\mathbf{O}} \end{bmatrix} = \begin{bmatrix} \left[\mathbf{R}^{(\mathbf{m})}\right] \\ \begin{bmatrix} \vec{U} \cdot \vec{\mathrm{n}} \,|_{S_B} & \text{for} & m = 1 \\ 0 & \text{for} & m \geq 2 \end{bmatrix} \\ [0] \end{bmatrix} \tag{3.1}$$

- **F** is the array of eigenfunctions for the spectral potential:

$$[\mathbf{F}] = \begin{bmatrix} e^{ik_0 x_1} e^{|k_0| y_1} & e^{ik_1 x_1} e^{|k_1| y_1} & \cdots & e^{ik_{N_x} x_1} e^{|k_{N_x}| y_1} \\ e^{ik_0 x_2} e^{|k_0| y_2} & e^{ik_1 x_2} e^{|k_1| y_2} & \cdots & e^{ik_{N_x} x_2} e^{|k_{N_x}| y_2} \\ \vdots & \vdots & \ddots & \vdots \\ e^{ik_0 x_{N_x}} e^{|k_0| y_{N_x}} & e^{ik_1 x_{N_x}} e^{|k_1| y_{N_x}} & \cdots & e^{ik_{N_x} x_{N_x}} e^{|k_{N_x}| y_{N_x}} \end{bmatrix} \tag{3.2}$$

- $\left[\mathbf{F}'_{\mathbf{B}}\right]$ represents the influence of the spectral potential on the body:

$$\left[\mathbf{F}'_{\mathbf{B}}\right] = [\nabla(\ ) \cdot \vec{\mathbf{n}}]_{S_B} \tag{3.3}$$

- $\left[\mathbf{F}'_{\mathbf{O}}\right]$ represents the influence of the spectral potential on the bottom:

$$\left[\mathbf{F}'_{\mathbf{O}}\right] = [\nabla(\ ) \cdot \vec{\mathbf{n}}]_{S_O} \tag{3.4}$$

- $[\mathbf{L}_{\mathbf{BW}}]$ defines the influence of the body potential on the spectral potential *on y=0*
- $[\mathbf{L}_{\mathbf{OW}}]$ defines the influence of the bottom potential on the spectral potential *on y=0*
- $[\mathbf{L}_{\mathbf{BB}}]$ defines the body's self-influence
- $[\mathbf{L}_{\mathbf{OB}}]$ defines the influence of the bottom potential on the body
- $[\mathbf{L}_{\mathbf{BO}}]$ defines the influence of the body potential on the bottom
- $[\mathbf{L}_{\mathbf{OO}}]$ defines the bottom's self-influence
- $\left[\mathbf{\Phi}_{\mathbf{sp}}{}^{(m)}\right]$ is the array of spectral potential modal amplitudes, $A_n(t)$
- $\mathbf{\Phi}_{\mathbf{B}}{}^{(m)}$ is the body potential
- $\mathbf{\Phi}_{\mathbf{O}}{}^{(m)}$ is the bottom potential

Note that $[\mathbf{L}_{\mathbf{OO}}]$ and $[\mathbf{L}_{\mathbf{OW}}]$ need to be computed only once.

- $\left[\mathbf{R^{(m)}}\right]$ is the function representing the Dirichlet boundary conditions for $\Phi_{sp}^{(m)}$:

$$\begin{aligned} \mathbf{R}^{(1)} &= \Phi^S \\ \mathbf{R}^{(m)} &= -\sum_{k-1}^{m-1} \frac{\eta^k}{k!} \frac{\partial^k}{\partial y^k} \phi_T^{(m-k)}(x,0,t) \end{aligned} \tag{3.5}$$

where $\phi_T^{(m-k)}(x,0,t) = \phi_{sp}^{(m-k)}(x,0,t) + \phi_B^{(m-k)}(x,0,t) + \phi_O^{(m-k)}(x,0,t)$.

Note that all the $[\mathbf{L}]'s$ contain the influences of the sources and their negative images.

For deep water, 3.1 is rewritten as:

$$\begin{bmatrix} [\mathbf{F}] & [\mathbf{L_{BW}}] \\ \left[\mathbf{F'_B}\right] & [\mathbf{L_{BB}}] \end{bmatrix} \begin{bmatrix} \left[\mathbf{\Phi_{sp}^{(m)}}\right] \\ \mathbf{\Phi_B^{(m)}} \end{bmatrix} = \begin{bmatrix} \left[\mathbf{R^{(m)}}\right] \\ \begin{bmatrix} \vec{U} \cdot \vec{\mathrm{n}} \mid_{S_B} & \text{for} \quad m = 1 \\ 0 & \text{for} \quad m \geq 2 \end{bmatrix} \end{bmatrix} \tag{3.6}$$

The body potential is represented as a horizontally periodic array of sources with negative images reflected about the mean free surface, $y = 0$. When present, the bottom can be similarly represented. A consequence of this choice is that the $[\mathbf{L_{BW}}]$ and $[\mathbf{L_{OW}}]$ matrices are identically zero. It is noted that this construction may appear similar to the 'pressure release' problem, the high-frequency limit of the linear free surface boundary condition (cf. Newman [33]). However, in that linearized problem the complete solution yields $\Phi(x,0,t) = 0$ whereas this is not the case for the problem at hand. The negative images here are used to provide computational efficiency without restricting the generality of the solution. In particular it permits fast calculation for the spectral potential at each time step.

3.2 Computational Steps

The time simulation of wave-body interactions, developed here for the deep water case for simplicity, proceeds as follows:

1. Initial conditions ($t = 0$) are specified for:

   The free surface profile, $\eta(x,t)$;

   Free surface potential, $\Phi^{\mathbf{S}}(x,t)$; and

   Body position and velocity, $S_B(x,y,t)$ and $\mathbf{U}(x,y,t)$,.

2. The boundary value problem is solved for the spectral potential, $\phi_{sp}^{(m)}$, and the source strength distribution on the body, $\sigma_{S_B}^{(m)}$. For the first set of computations, at $m = 1$:

   a. The spectral potential is determined by solving the following for $\phi_{sp}^{(m)}$:

$$[\mathbf{F}]\left[\Phi_{\mathbf{sp}}^{(\mathbf{m})}\right] = \left[\mathbf{R}^{(\mathbf{m})}\right] \tag{3.7}$$

   b. With the spectral potential at a given order known, the source strengths are determined by solving

$$\left[\mathbf{F}_{\mathbf{B}}^{'}\right]\left[\Phi_{\mathbf{sp}}^{(\mathbf{m})}\right] + \left[\mathbf{L}_{\mathbf{BB}}\right]\left[\Phi_{\mathbf{B}}^{(\mathbf{m})}\right] = \begin{bmatrix} \vec{U}\cdot\vec{\mathrm{n}}\,|_{S_B} & \text{for} \quad m=1 \\ 0 & \text{for} \quad m \geq 2 \end{bmatrix} \tag{3.8}$$

   The above steps (2.a and 2.b) are repeated up through perturbation order M. The body contributes to $\phi_{sp}^{(m)}$ through its vertical derivatives.

3. Compute the quantities necessary for the time integration of the free surface boundary conditions. These quantities are:

   $\Phi_y(x, \eta(x,t), t)$;

   $\Phi_x^S(x,t)$; and

   $\eta_x(x,t)$.

4. Integrate the free surface boundary conditions, equations (2.12) and (2.13), to update the free surface potential, $\Phi^S(x,t)$, and free surface elevation, $\eta(x,t)$

Steps 2, 3, and 4 are repeated at each time step.

The following section details the manner in which each of the above steps is performed.

3.3 Solution of the Boundary Value Problem

Initial Conditions- Free Surface Elevation and Potential

The solution of the nonlinear wave body interaction problem requires the free surface elevation and potential to be accurately specified. The free surface profile and velocity potential used here for initial conditions are generated by Stokes' expansions. The mapped equations of Schwartz [41] are used to specify a Stokes' Wave of arbitrary order N [22]. For the typical wave-body interaction analyzed in this thesis $N = 20$ is sufficient for specifying the initial free surface profile and velocity potential. The differences in the free surface profile for expansions of order 2, 10 ,and 20 are shown in Figure 3-1.

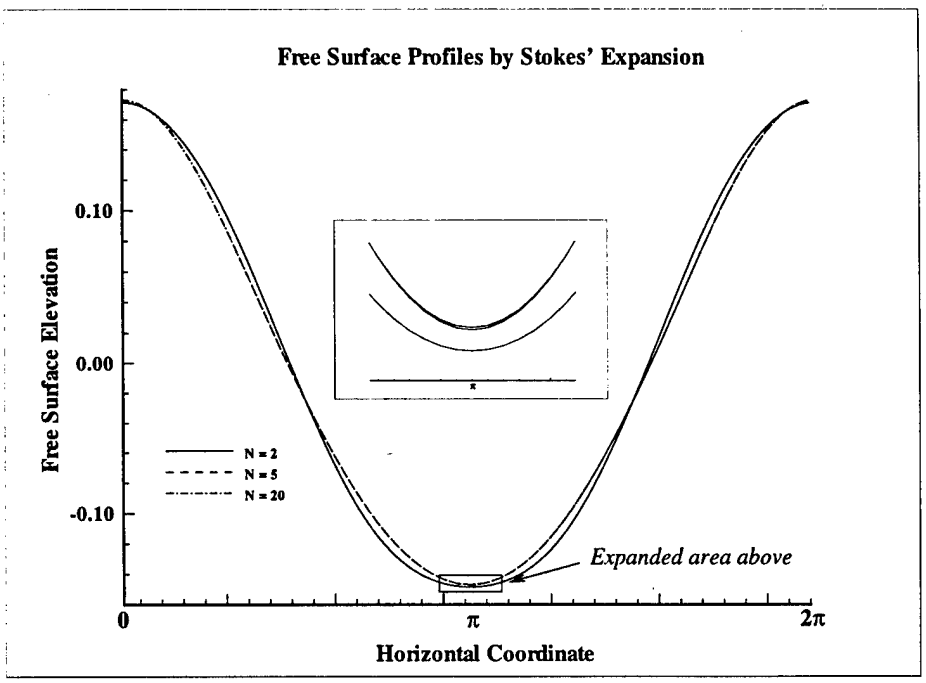

Figure 3-1: Initial free surface profile

Though the calculations done here are for Stokes' waves as initial conditions, the equations and solution methods apply to fully arbitrary initial conditions.

Influence Coefficient Matrices: [F] and $\left[\mathbf{F}_{\mathbf{B}}^{'}\right]$

The spectral potentials at each order, $\phi_{sp}^{(m)}$, are obtained by solving equation 3.7 for the Fourier modal amplitudes, $A_n(t)$. In expanded form:

$$\phi^{(m)}(x,0,t) = \sum_{n=0}^{N_x} A_n(t) e^{ik_n x} =$$

$$\begin{cases} \Phi^S(x,t) & m = 1 \\ -\sum_{k=1}^{m-1} \frac{\eta^k}{k!} \left[\frac{\partial^k}{\partial y^k} \left(\phi_{sp}^{(m-k)}(x,y,t) + \phi_B^{(m-k)}(x,y,t) \right) \right]_{y=0} & m \geq 2 \end{cases} \tag{3.9}$$

The higher order spectral potentials are functions of the free surface elevation and vertical derivatives of the lower order potentials evaluated on the mean free surface. The vertical derivatives are obtained by computing the modal amplitudes of the lower order potentials by Fast Fourier Transform (FFT), multiplying the modal amplitudes by $|k_n|$, and generating the derivatives in physical space by inverse FFT:

$$\frac{\partial^l \phi_{sp}^{(m)}}{\partial^l y} = \sum_{n=1}^{N} |k_n|^l e^{ik_n x} e^{|k_n| y} \Big|_{y=0} \tag{3.10}$$

The products needed in the boundary conditions for the spectral potentials, e.g.,

$$\eta(x) \frac{\partial \phi^{(1)}}{\partial y}(x,0,t) \tag{3.11}$$

are formed in physical space. The operational count associated with obtaining each $\phi_{sp}^{(m)}$ is $O(N_x \log N_x)$.

With the Fourier amplitudes of the spectral potentials known, the spectral potential and its derivatives can be determined throughout the fluid domain. In particular, the influence of the spectral potential on the body is computed directly from

$$\left[\mathbf{F}'_{\mathbf{B}}\right]\Phi_{\mathbf{sp}}^{(\mathbf{m})} = \left[\nabla\Phi_{\mathbf{sp}}^{(\mathbf{m})}\cdot\vec{\mathbf{n}}\right]_{S_B} = \begin{bmatrix} A_0(t)\left((ike^{ik_0x_i})\vec{\mathbf{i}} + (|k_0|e^{|k_0|y_i})\vec{\mathbf{j}}\right)\cdot\mathbf{n_B} \\ A_1(t)\left((ike^{ik_1x_i})\vec{\mathbf{i}} + (|k_1|e^{|k_0|y_i})\vec{\mathbf{j}}\right)\cdot\mathbf{n_B} \\ A_2(t)\left((ike^{ik_2x_i})\vec{\mathbf{i}} + (|k_2|e^{|k_0|y_i})\vec{\mathbf{j}}\right)\cdot\mathbf{n_B} \\ \vdots \\ A_{N_x}\left((ike^{ik_{N_x}x_i})\vec{\mathbf{i}} + (|k_{N_x}|e^{|k_{N_x}|y_i})\vec{\mathbf{j}}\right)\cdot\mathbf{n_B} \end{bmatrix} \tag{3.12}$$

x_i, y_i are the locations of the N_B body segment midpoints.

The operational count associated with determining the influence of the spectral potential on the body is $O(N_xN_B)$. The influence of the spectral potential on the body is combined with the body boundary condition to form the right hand side for the equation to be solved for the source distribution on the body:

$$[\sigma(x_i,y_i,t)] = [\mathbf{L_{BB}}]^{-1}\begin{bmatrix} \left(\vec{U}\cdot\vec{\mathbf{n}} - \left[\mathbf{F}'_{\mathbf{B}}\right]\phi_{sp}^{(m)}\right) & m=1 \\ -\left[\mathbf{F}'_{\mathbf{B}}\right]\phi_{sp}^{(m)} & m\geq 2 \end{bmatrix} \tag{3.13}$$

Equation (3.13) is solved by factoring the body-body influence coefficient matrix, $[\mathbf{L_{BB}}]^{-1}$, and determining the source strengths by back substitution. The body-body influence coefficient matrix must be factored only once, at the first time step. The operational count associated with solving 3.13 at the first time step is $O(N_B^3)$. The operational count at subsequent time steps is $O(N_BN_B)$.

Equation 3.13 requires derivatives of the form

$$\frac{\partial^k \phi_B^{(m-k)}}{\partial^k y}(x,0,t)\,, \quad k=1,2,\ldots,m-1 \tag{3.14}$$

$\partial\phi_B^{(m)}(x,0,t)/\partial y$ is computed using the analytical expression for the representation of the body as a distribution of periodic sources and their negative images. Higher derivatives are found through the use of Laplace's equation ([8]). For example, $\left(\partial^3\phi_B^{(1)}/\partial y^3\right)|_{y=0}$ is required for the solution of the fourth order problem. $\partial\phi_B^{(1)}/\partial y$ is a harmonic function, therefore

$$\frac{\partial^2}{\partial y^2}\left(\frac{\partial\phi_B^{(1)}}{\partial y}\right) = -\frac{\partial^2}{\partial x^2}\left(\frac{\partial\phi_B^{(1)}}{\partial y}\right) \tag{3.15}$$

$\partial\phi_B^{(1)}/\partial y$ is computed as before and the horizontal derivatives are computed numerically. The symmetry properties of the body-image system force the even numbered vertical derivatives to be zero.

After the initial set up effort, the total operational count associated with solving the boundary value problem to order M at each time step is

$$O(M[N_x \log(N_x) + N_x N_B + N_B N_B]) \tag{3.16}$$

The total operational count of the High Order Spectral Method (HOSM) of Liu, Dommermuth, and Yue [23] is

$$O(M[N_x \log(N_x) + N_x N_B + N_B \log N_B]) \tag{3.17}$$

As in the HOSM, typically $N_x \gg N_B$. Thus, for large numbers of panels the new method is slower than the full spectral method, but provides the benefit of allowing completely arbitrary body geometries.

3.4 Updating the Free Surface Potential and Elevation

The Zakharov equations (equations 2.12 and 2.13) are used as time evolution equations for the free surface elevation $\eta(x,t)$, and the free surface potential $\Phi^S,(x,t)$. The time integration requires (a) the accurate determination of the spatial derivatives of the free surface elevation η_x, free surface potential ϕ_x^S, and velocity potential ϕ_y, and (b) a stable and accurate time integration scheme.

Horizontal Derivatives of $\eta(x,t)$ and $\phi^S(x,t)$

The free surface elevation and free surface potential are defined at evenly spaced points along the x axis. The horizontal derivatives of these quantities are most efficiently performed in Fourier space:

$$\frac{\partial \eta(x,t)}{\partial x} = \sum_{n=0}^{N_x} B_n(t) i k_n e^{i k_n x} \tag{3.18}$$

$$\frac{\partial \phi^S(x,t)}{\partial x} = \sum_{n=0}^{N_x} A_n^S(t) i k_n e^{i k_n x} \tag{3.19}$$

where $B_n(t)$ and $A_n^S(t)$ are the Fourier amplitudes of the free surface elevation and potential respectively. The operational count associated with computing these spatial derivatives is $O(N_x \log N_x)$. Products involving these quantities are computed in physical space.

The Vertical Velocity of the Fluid on the Free Surface

The vertical velocity of the fluid on the free surface is the sum of the contribution from the spectral potential and the body potential. The contribution from the spectral potential is determined by computing the derivatives in Fourier space [8]:

$$\frac{\partial^{k+1}}{\partial y^{k+1}}\Psi_n(x,y)|_{y=0} = |k_n|^{k+1}\Psi_n(x,y)|_{y=0} \tag{3.20}$$

The Fourier amplitudes are found by FFT and the appropriate power of the wave number is multiplied by the series representation of the function, and the required derivative of the function is computed by the inverse FFT. The operational count associated with computing these derivatives is $O(N_x \log N_x)$.

The contribution, at each order, of the body potential to the fluid vertical velocity on the free surface is computed using the derivative of analytical expression for the potential due to the body and its negative image.

The operational count associated with computing the vertical derivatives is $O(N_x N_B)$. The total operational count associated with computing the terms required for solution of the kinematic and dynamic free surface boundary conditions is $O(M[N_x \log N_x + N_x N_B + N_B N_B])$.

The above steps provide the information required to compute $\partial\eta(x,t)/\partial t$ and $\partial\phi^S(x,t)/\partial t$ at each time step. In the next section the method used to integrate the free surface evolution equations in time is presented.

Time Integration

The integration scheme used to evolve the free surface shape and free surface potential is a fourth order Runge-Kutta (RK4) scheme. The stability properties of this method as applied to the non-linear wave body interaction problems were developed by Dommermuth

[7] and used by Liu [22] in his extension of Dommermuth's work. The important points from Dommermuth are:

1. RK4 is conditionally stable;

2. The Courant condition for RK4, based on von Neumann stability analysis of the linearized free surface conditions, is $g\, k_{grid} \Delta t^2 \leq 8, \quad k_{grid} = 2\pi/\Delta x$; and

3. RK4 is mildly dissipative.

Analyses of other time integration schemes for numerical simulations of wave-wave and wave-body interactions are found in Kring [20] and Dommermuth [7].

Considerable information is available concerning the development and growth of "saw-tooth instabilities" in time simulations of free surface flows. Olmez [37] and Dommermuth [7] provide comprehensive background discussions of the saw-tooth instability. Longuet-Higgins and Cokelet [25] were the first to report the presence of the sawtooth instability and contended that its presence was partly physical. Other investigators reporting sawtooth type instabilities are Baker et al. [1], Lin et al. [21], and Sen et al. [42].

Dommermuth [7] and Roberts [39] stated that the sawtooth instabilities are numerical. Olmez [37] stated that the cause of the instability is unknown.

The discretization of the physically continuous problem introduces a sawtooth wave form at the highest resolvable wave number, $k = 2\pi/\Delta x$ (Figure 3-2).

The coupling provided by the method of solution outlined in the previous chapter ensures that all modes at all orders are coupled. Instabilities at any mode are coupled to all other modes. The presence of physical or numerical stabilizing mechanisms determines whether a given frequency is stable. In the chosen mathematical formulation of the physical problem the fluid is assumed to be ideal. Therefore no physical dissipative mechanism exists. The

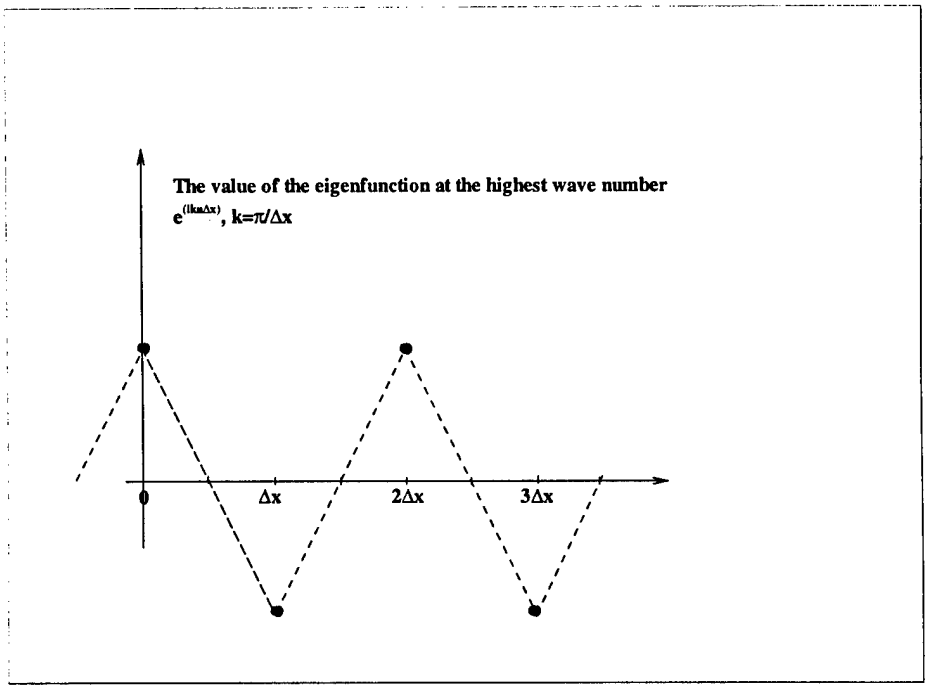

Figure 3-2: Sawtooth at Highest Wavenumber

numerical scheme must provide the dissipation absent in the chosen physical model. RK4 is mildly dissipative.

The level of accuracy of the spatial derivatives evaluated on the free surface influences the onset of sawtooth instabilities (Roberts [39] and Dommermuth [7]). Derivatives of the potential of each order m are of the form

$$\frac{\partial^m}{\partial y^m}\Psi_n = |k_n|^m \Psi_n \tag{3.21}$$

where n is the Fourier mode. The magnitude of the derivative is proportional to $(k_n)^m$. The error at a given mode and order is amplified by this factor [7]. If dissipation is not provided the growth of this error can be unbounded. Longuet-Higgins [25], Dommermuth [7], and Liu [22] all use a form of smoothing to further control high wave number instabilities. In this thesis an ideal low pass filter is used to remove the highest wave number modes. The cutoff

wave number is constrained by physical considerations. The filter must allow physically relevant waves to develop, $\lambda_{cutoff}/D_{body} \ll 1$ and must not remove appreciable energy from the system. The filter is implemented by transforming the free surface elevation and free surface potential into the frequency domain by the FFT. All modes above the cutoff wave number are removed, and the filtered free surface elevation and potential are generated by inverse FFT.

3.5 Convergence

The Lax-Richtmyer equivalence theorem states that a consistent approximation to a well-posed linear problem is stable if and only if it is convergent [10]. First, it is necessary to demonstrate that the numerical solution method is consistent. The consistency is demonstrated by conservation of volume and conservation of energy. Confidence in converged results is provided by comparison of converged results with experimental results and results generated by other numerical methods (Cointe [6]) .

Energy and Volume Conservation

Volume conservation requires

$$\int_{S_F(t)} \eta(x,t)\, dx = \text{Constant} \tag{3.22}$$

Energy conservation requires

$$\rho \int\int\int_{\mathcal{V}} \left(\frac{1}{2}V^2 + gy\right) d\mathcal{V} = \mathcal{L} \tag{3.23}$$

A convenient form of the total energy can obtained by making use of the kinematic information, $\mathbf{U} = \nabla\phi$ and $\nabla^2\phi = 0$ and the first form of Green's theorem

$$\int_{\mathcal{V}} \left[\phi\nabla^2\phi + (\nabla\phi)^2\right] d\upsilon = \int_S \mathbf{n} \cdot \phi\nabla\phi ds \tag{3.24}$$

The above information can be used to express the kinetic energy T as (Milder [28] and Kinsman [18]

$$T = \frac{1}{2}\rho \int \nabla\phi \cdot \nabla\phi d\upsilon = \frac{1}{2}\rho \int \phi\nabla\phi \cdot ds = \frac{1}{2}\rho \int \phi^S \eta_t\, dx \tag{3.25}$$

The expression used for computing the total energy, $\mathcal{L}$, in the system is

$$\mathcal{L} = \frac{1}{2}\rho \int \phi^S \eta_t\, dx + \frac{1}{2}\rho g \int \eta^2\, dx \tag{3.26}$$

The total energy is computed at each time step.

Convergence- Discussion

The convergence properties of the combined HOSM-BIEM method are functions of the following sources of error [7] :

1. Finite numbers of body segments N_B, Fourier modes N_x, and perturbation order M ;
2. Time integration scheme;
3. Finite computational domain;
4. Filter cutoff wave number N_{filter}; and
5. Aliasing.

The first four sources of error require no explanation. The convergence properties associated with each will be examined in the subsequent section.

Solutions associated with wave numbers above the highest grid wave number ($k = 2\pi/\Delta x$) can not be distinguished from waves of lower frequency [46]. This is aliasing and it occurs is when products are formed in the spectral method, e.g., $\eta_x \eta_x$

$$\sum_{n=0}^{N_x} \eta_{n(t)} e^{ik_n x} ik_n \sum_{n=0}^{N_x} \eta_{n(t)} e^{ik_n x} ik_n = -k_0^2 \left(\eta_0(t)\right)^2 e^{2ik_0 x} + \ldots + -k_{N_x}^2 \left(\eta_{N_x}\right)^2 e^{2k_{N_x}} \quad (3.27)$$

Products are made alias free using the method developed by Orszag [38].

Convergence- Demonstration

The convergence properties of the HOSM-BIEM are demonstrated in this section.

Nomenclature:

- M = Perturbation order
- N_B = Number of body segments
- $\bar{F}_y$ = Steady vertical force
- ρ = Fluid density
- g = Gravitational constant
- A = Wave amplitude
- k = Wave number
- R = Body radius
- H = Distance from mean free surface to center of body
- N_W = Domain size; the number of waves of the fundamental wave length in the domain
- N_x = Number of Fourier modes; equal to the number of segments along the x axis
- T = Period of the fundamental wave
- T_S = Simulation time
- Δt = Time step size
- N_{filter} = Fourier mode for low pass filter cut-off

N_B	$M=2$	$M=3$	$M=4$
64	0.2807	0.2799	0.2798
128	0.2783	0.2775	0.2775
256	0.2768	0.2760	0.2760

Table 3.1: Convergence of the vertical drift force, $\bar{F}_y/\rho g A^2$, with body segments N_B and order M. $kA = 0.04$, $kR = 0.4$, and $H/R = 2$; and $N_W = 16$, $N_x = 64N_W$, $N_{filter} = 24N_W$ for $N_B = 64$ and $N_B = 128$, $N_{filter} = 32N_W$ for $N_B = 256$, $T/\Delta t = 128$, $T_S = 5T$.

Table 3.1 shows the convergence of the vertical drift force with increasing number of body segments N_B and perturbation order M. The convergence rate appears to be better than linear with increasing number of body segments, and exponential with increasing perturbation order. The full spectral method of Dommermuth converges exponentially with increasing number of body modes (segments). The combined method of this thesis uses a boundary integral representation for the body's contribution to the velocity potential. Therefore the convergence rate is not expected to match that of the full spectral method. The decreased convergence rate is a penalty associated with the improved flexibility of the present method.

Figure 3-3 shows the behavior of the solution for the vertical force as the value of the low-pass filter cut-off wave number is varied. The cut-off wave number corresponds to waves whose lengths vary from 2/3 to 1/48 of the wavelength of the fundamental of the initial Stokes wave. For cut-off wave numbers corresponding to waves shorter than 1/4 of the fundamental, there is no appreciable change in the vertical drift force.

Table 3.2 shows the convergence of the vertical drift force with increasing number of Fourier modes and perturbation order. The convergence rate appears to be exponential with increasing number of Fourier modes and exponential with increasing perturbation order.

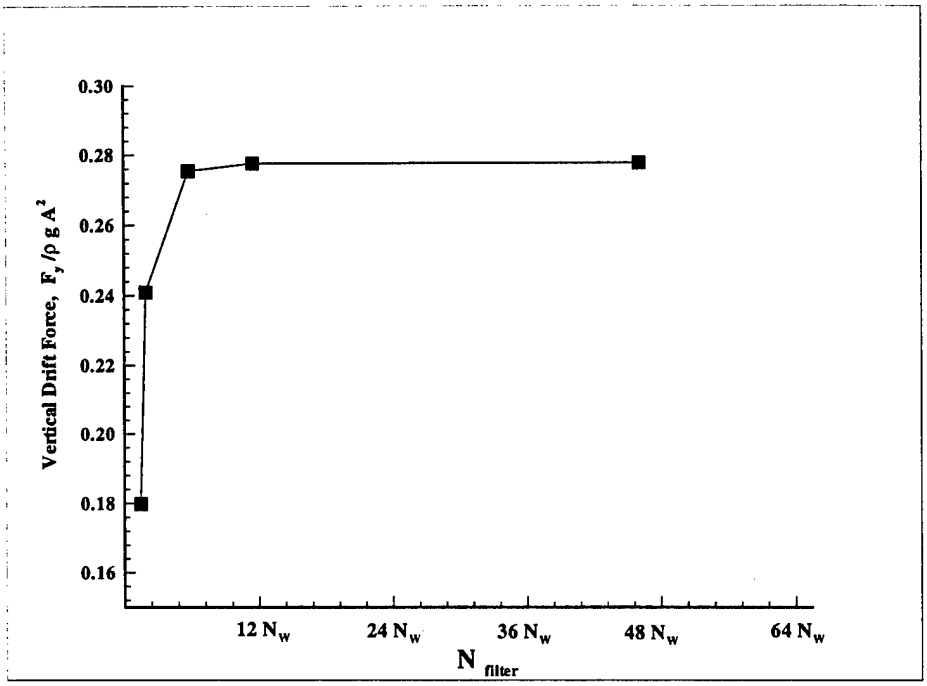

Figure 3-3: Behavior of the vertical drift force, $\bar{F}_y/\rho g A^2$, with varying cut-off wave number N_{filter}. $kA = 0.04$, $kR = 0.4$, and $H/R = 2$; and $N_B = 256$, $N_W = 16$, $N_x = 64N_W$, $T/\Delta t = 128$, $M = 4$, $T_S = 3T$.

Table 3.3 shows how the convergence of the vertical drift force varies with increasing wave slope. The convergence rate with increasing number of Fourier modes decreases as the wave slope increases. $N_x = 32N_W$ Fourier modes was insufficient for $kA = 0.12$. The number of Fourier modes was insufficient to resolve the local steep waves in the vicinity of the body and the numerical solution broke down after 2 wave periods.

Table 3.4 shows the convergence of the method with respect to time step size. The behavior of the solution with time step size is consistent with the findings of Korsmeyer [19]. For solutions that are converged with respect to the spatial variables, there is a wide range of solutions for which changes in time step size do not affect the accuracy of the solution. For larger time step sizes the solution error grows rapidly and is unstable [19].

ϵ	N_x	$M=2$	$M=3$	$M=4$
0.04	32 N_W	0.2769	0.2758	0.2760
	64 N_W	0.2768	0.2760	0.2760
	128 N_W	0.2768	0.2760	0.2760

Table 3.2: Convergence of the vertical drift force, $\bar{F}_y/\rho g A^2$, with Fourier modes N_x and order M. $kR = 0.4$, and $H/R = 2$; and $N_W = 16$, $N_{filter} = 24N_W$, $N_B = 256$, $T/\Delta t = 128$, $T_S = 5T$.

ϵ	32 N_W	64 N_W	128 N_W
0.04	0.2760	0.2760	0.2760
0.08	0.2760	0.2706	0.2706
0.12	-	0.2692	0.2640

Table 3.3: Convergence of the vertical drift force, $\bar{F}_y/\rho g A^2$, with Fourier modes N_x as wave slope kA increases. $M = 4$, $kR = 0.4$, and $H/R = 2$; and $N_W = 16$, $N_{filter} = 24N_W$, $N_B = 192$, $T/\Delta t = 128$, $T_S = 3T$.

Figure 3-4 shows the behavior of the HOSM-BIEM method as the domain size is varied. The purpose of evaluating the behavior of the solution as the domain size varies is to determine the influence of the periodic problem formulation on the ability to achieve and sustain limit-state behavior before "reflections" from the periodic boundaries effect the solution. Figure 3-4 shows that limit state behavior is reached within 3 periods, $T_S = 3T$, of simulation time. The effect of "reflections" for $N_W = 8$ is evident in Figure 3-4.

$T/\Delta t$	$M=2$	$M=3$	$M=4$
32	0.27826	0.2775	0.2774
64	0.2783	0.2775	0.2775
128	0.2783	0.2775	0.2775

Table 3.4: Convergence of the vertical drift force, $\bar{F}_y/\rho g A^2$, with time step size $T/\Delta t$ and order M. $kA = 0.04$, $kR = 0.4$, and $H/R = 2$; and $N_W = 16$, $N_{filter} = 24N_W$, $N_F = 64N_W$, $N_B = 128$, $T_S = 5T$.

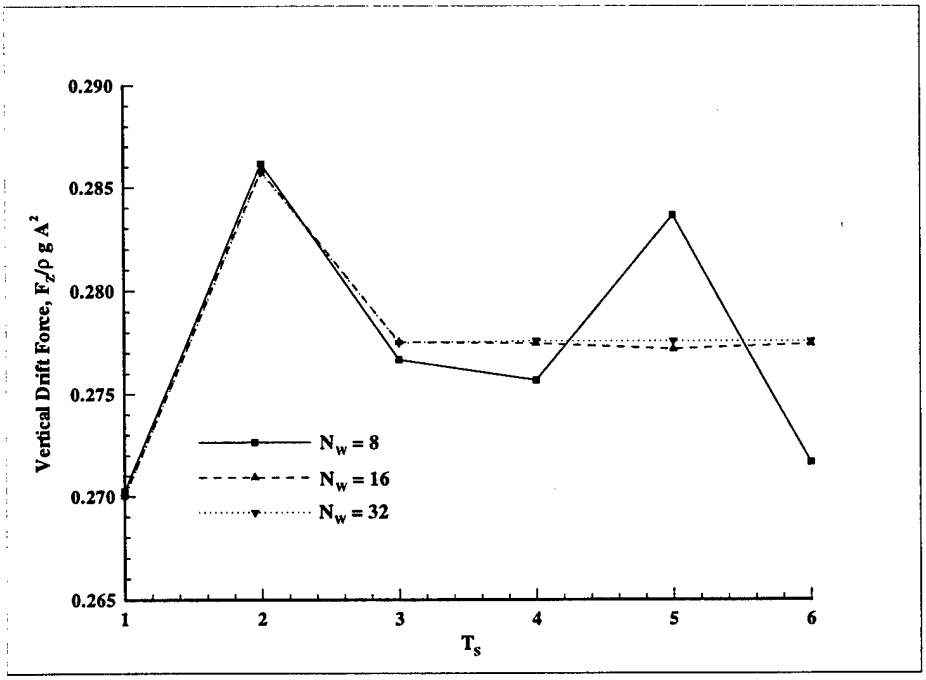

Figure 3-4: Behavior of the vertical drift force, $\bar{F}_y/\rho g A^2$, with varying domain size N_W where N_W is the ratio of the domain size to the fundamental wavelength. $kA = 0.04$, $kR = 0.4$, and $H/R = 2$; and $N_B = 128$, $N_x = 64N_W$, $N_{filter} = 24N_W$, $T/\Delta t = 128$, $M = 4$

Chapter 4

Wave Diffraction by Submerged Cylinders

The purpose of this chapter is to present the results for the analysis of the diffraction of incident waves by submerged circular cylinders. The diffraction of waves by cylinders of circular and 'pontoon' cross sections are studied. The pontoon case is analyzed to demonstrate the applicability of the method to arbitrary geometric shapes. Figure 4-1 defines the problem parameters.

The oscillatory and steady forces for a range of problem parameters are presented and compared with related results generated from the other solution methods and experimental results discussed in Chapter 1.

4.1 Diffraction by a Cylinder of Circular Cross Section

The forces resulting from the interaction of a fully submerged circular cylinder with Stokes' waves are analyzed in this section. The forces on the cylinder are evaluated as functions of:

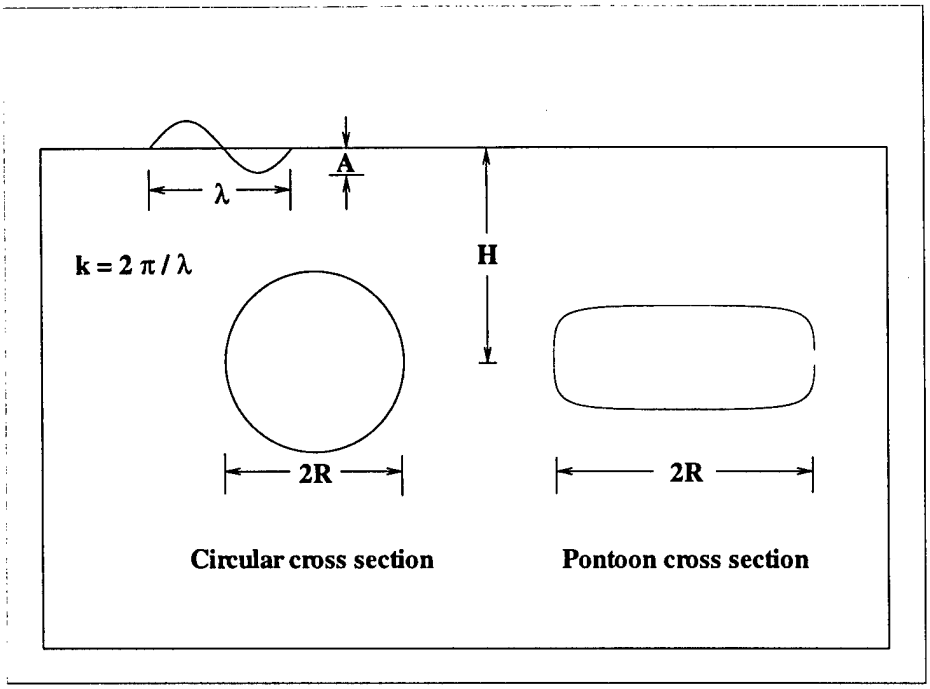

Figure 4-1: Diffraction problem parameters

- Keulegan-Carpenter number, $K_C = \pi e^{-kH} A/R$;
- Wave slope, kA ; and
- Submergence ratio, $h = H/R$.

Although a "natural" nondimensional variable is kR, the variable K_C, which is equivalent in the presence of the other nondimensional variables, is used instead to make the results directly comparable to others in the literature.

The forces analyzed are:

- First, second, and third harmonics of the vertical and horizontal forces, and
- Steady vertical and horizontal forces.

Method of Computing Forces

Time simulations of the initial boundary value problems are performed long enough for the solution to achieve limit-state behavior and terminated when "reflections" from the domain boundaries begin to influence the solution. Limit state behavior is typically reached within two periods. The length of time the limit-state behavior is sustained is determined by domain width, N_W (see figure 3-4). For the diffraction problem the forces are computed by applying Equations 2.29 and 2.30 to the time history of the sum of the potentials at each order, $\Phi_T^{(m)}, m = 1, 2, \ldots, M$, to generate a force time history. For stationary bodies the equations reduce to

$$F(t) = -\rho \int_{S_B} p(t)\,\mathbf{n}\,dS = -\rho \int_{S_B} \left[\frac{\partial \phi_T(t)}{\partial t} + \frac{1}{2}\nabla\phi_T(t)\cdot\nabla\phi_T(t)\right]\mathbf{n}\,dS \tag{4.1}$$

where $\phi_T(t)$ is the total potential on the body's surface.

For the circle Equation 4.1 becomes

$$F(t) = -\rho \int_{S_B} \left[\frac{\partial \phi_T(t)}{\partial t} + \frac{1}{2}\left(\frac{1}{r_o}\frac{\partial \phi_T(t)}{\partial \theta}\right)^2\right]\mathbf{n}\,dS \tag{4.2}$$

where r_o is the circle radius.

Numerically,

$$F(t) = -\rho \sum_{i=1}^{N_B} \left[\frac{\partial \phi_{i_T}(t)}{\partial t} + \frac{1}{2}\left(\frac{1}{r_o}\frac{\partial \phi_{i_T}(t)}{\partial \theta}\right)^2\right]\mathbf{n_i}\,dS \tag{4.3}$$

$\partial\phi_{i_T}(t)/\partial t$ and $(\partial\phi_T(t)/\partial\theta)_i$ are computed by temporal and spatial central differencing, respectively. The potential and pressure along each segment are assumed to be constant. Therefore the integrated quantity at each time step is computed as the simple sum,

$$\sum_{i=1}^{N_B} p_i n_i dS_i \tag{4.4}$$

The force at each order m is related to the n^{th} harmonic coefficient of the force:

$$F_n = F^{(m)} \sim \frac{1}{T}\int_t^{t+T} F(t)e^{jm\omega t}dt; \qquad n = m = 1, 2, \ldots, M \tag{4.5}$$

with $j = \sqrt{-1}$.

The forces computed by the combined method are compared with solutions generated by the other methods described in Chapter 1. As noted by Liu, et al. [23], there is no direct relationship between the $F^{(m)}$ terms of the nonlinear solution and the $\tilde{F}_n = \sum_{m=1}^{\infty} \epsilon^m \tilde{\phi}_n^{(m)}$ terms of a perturbation series solution generated by a boundary condition perturbation frequency-domain approach. Liu et al. demonstrate that relationships between the nth-harmonic of the nonlinear solution, $\phi_n^{<M>} = \sum_{m=1}^{M} \phi_n^{(m)}$, $n = 1, 2, ..., N_x$ are related to the frequency domain amplitudes, $\Phi^{(n)}$ by

$$\tilde{\phi}_0^{(2)} = \phi_0^{<2>} + O(\epsilon^3) \tag{4.6}$$

$$\tilde{\phi}_n^{(n)} = \phi_n^{<M>} + O(\epsilon^{n+1}) \tag{4.7}$$

Numerical Results

In Figure 4-2 the first harmonic of the horizontal diffraction force on the submerged circular cylinder is shown as a function of the Keulegan-Carpenter number. The results are presented together with:

- The experiments of Chaplin [3] and Miyata [30];

- The linear theory of Ogilvie [35];
- The High-order Spectral Results (HOSM) of Liu, Dommermuth, and Yue [23]; and
- The Mixed Eulerian-Lagrangian (MEL) method of Cointe [6].

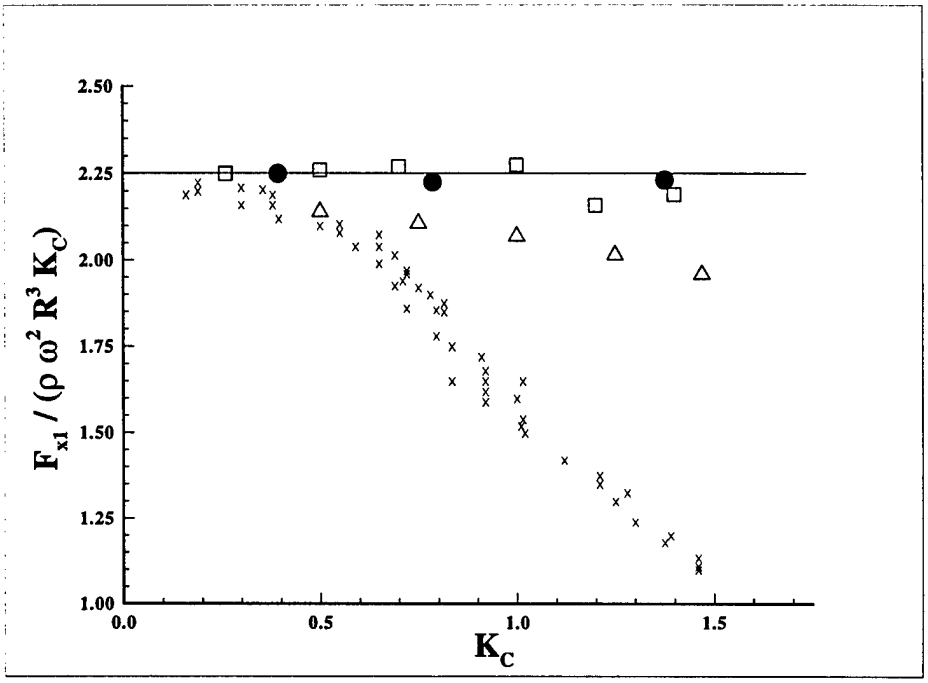

Figure 4-2: The first-harmonic of the horizontal diffraction force. Experiment (×); linear result(—); HOSM(□); MEL(△); present method (•). ($kR = 0.21$, $H/R = 2.0$.)

The agreement between the method developed in this thesis and the other numerical methods for this case helps to confirm the theoretical and numerical validity of the new method.

In Figure 4-2 the experimental results differ appreciably from the theoretical and numerical results at values of the Keulegan-Carpenter number greater than 0.5. The difference is due to flow separation, a fluid behavior not accounted for in the potential flow equations used in each of the theoretical and numerical methods cited.

The lack of agreement between the experimentally generated results and the results generated by the numerical methods is due to lift oscillating at the fundamental frequency in antiphase with the inertia force (Chaplin [3]). Chaplin's results were consistent with the analytical results of Longuet-Higgins [24] who computed the magnitude of the circulation associated with the oscillatory flow around the cylinder. The decrease in vertical force with increasing Keulegan-Carpenter number is due to the (negative)lift asscociated with the circulation.

The zeroeth, second, and third harmonics of the horizontal force are shown in Figures 4-3, 4-4, and 4-5 along with the results generated by experiments, second-order theory (Ogilvie [35]), perturbation theory (Vada [48]), and HOSM and MEL computations. The results of the theoretical and numerical methods agree with the experimental results over a wide range of Keulegan-Carpenter numbers.

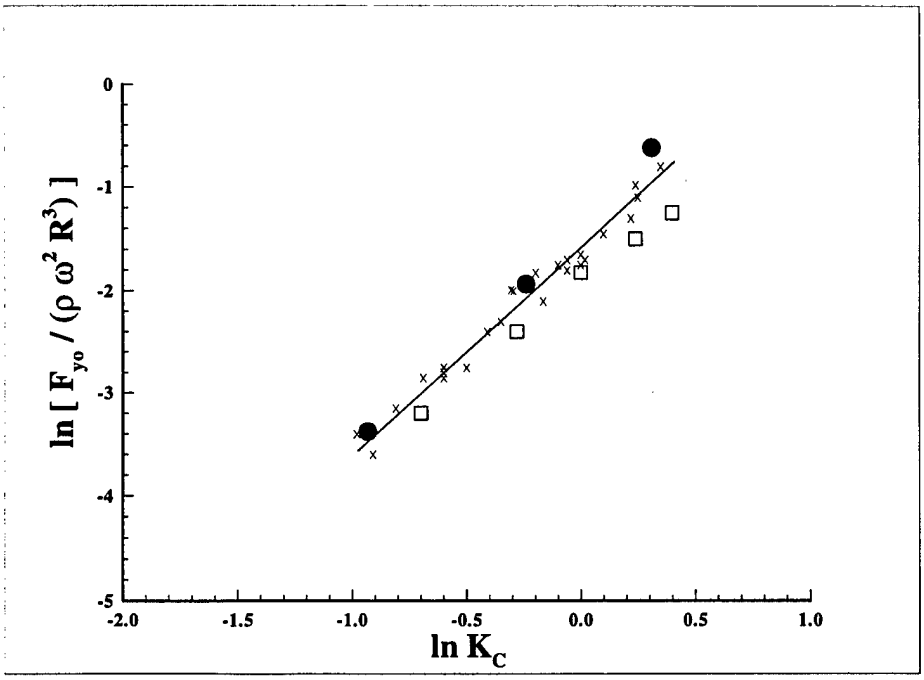

Figure 4-3: The steady vertical diffraction force. Experiment (×); MEL(□); second-order theory(—); present method(•). ($kR = 0.21$, $H/R = 2.0$.)

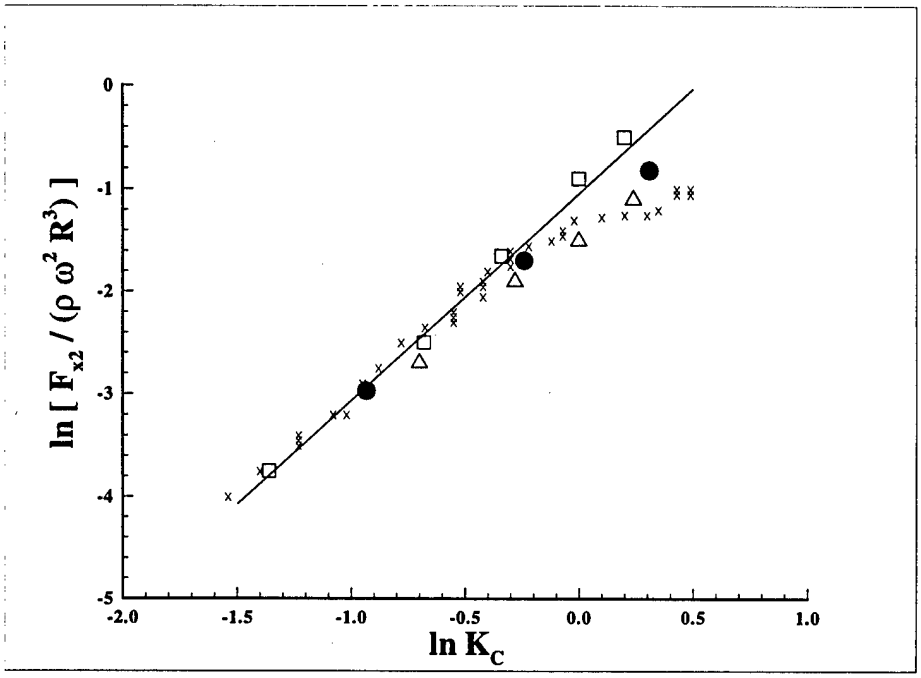

Figure 4-4: The second-harmonic of the horizontal diffraction force. Experiment (×); HOSM(□); MEL(△); perturbation theory(—), present method(•). ($kR = 0.21$, $H/R = 2.0$.)

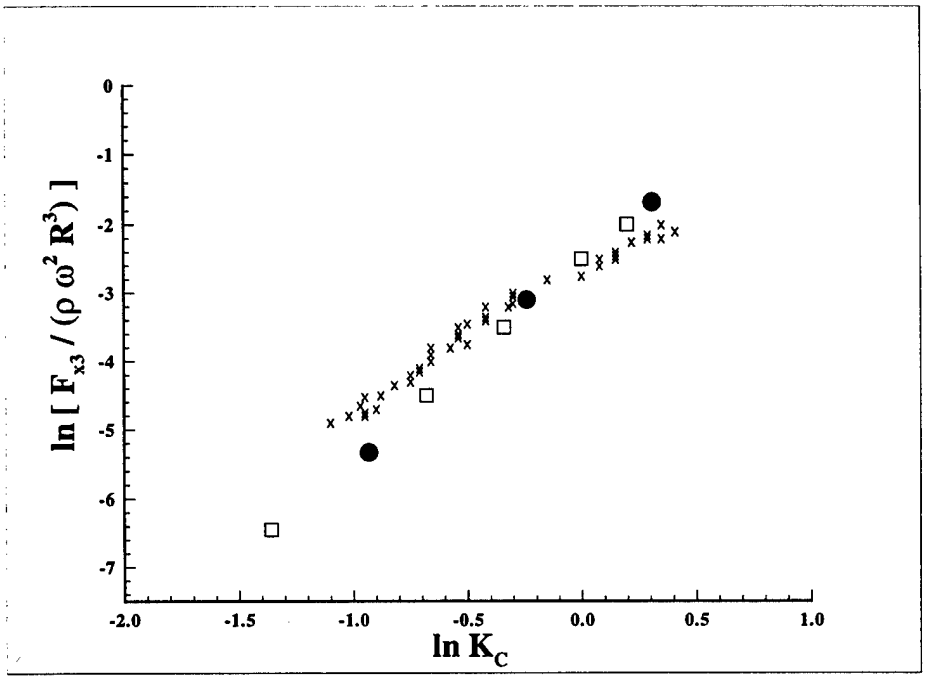

Figure 4-5: The third-harmonic of the horizontal diffraction force. Experiment (×); HOSM(□); present method(•). ($kR = 0.21$, $H/R = 2.0$.)

The drift forces as functions of wave slope are shown in Figure 4-6. The results of the present method are compared with those generated by the HOSM for the vertical force and the HOSM and MEL for the horizontal force. The normalized vertical drift force is independent of the wave slope. The normalized horizontal drift force is shown to decrease in magnitude as wave slope increases. The negative horizontal drift force was studied extensively by Dommermuth [7] and Liu et al. [23] and is not a principal focus of this thesis. Cointe [6] also computed a negative horizontal drift force. In Cointe's work the negative horizontal drift force is only present for wave steepnesses close to the limiting steepness of the method.

As wave slope becomes vanishingly small, the fourth order force should approach a constant. As seen in Figure 4-6 none of the numerical methods capture this result. The errors, however, for the high order spectral method and the present method are small.

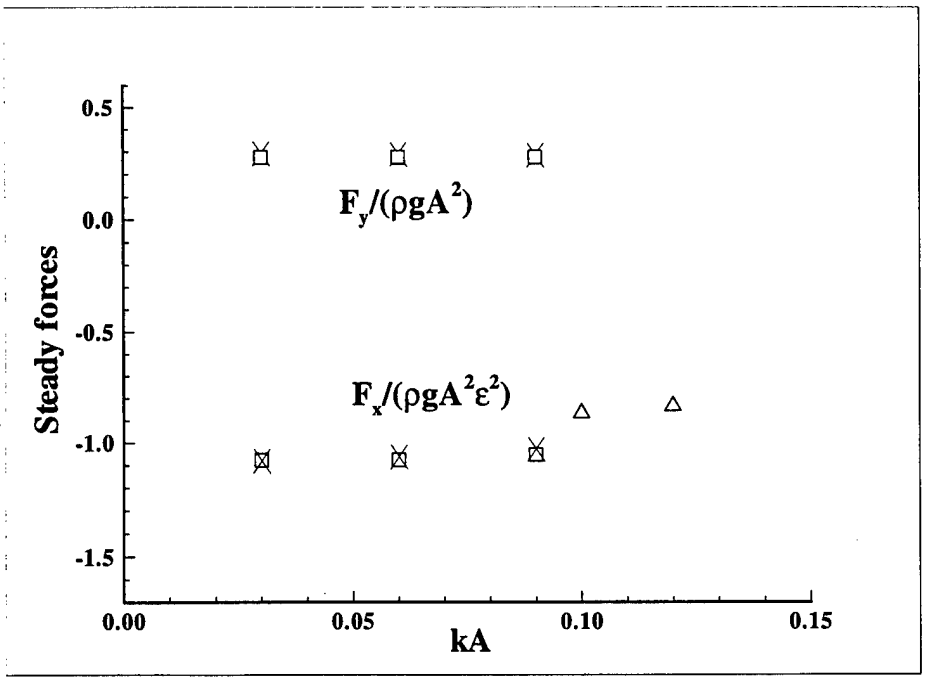

Figure 4-6: Drift forces as functions of wave slope, kA. F_y is the vertical force; F_x is the horizontal force. HOSM(□); MEL(△); present method(×). ($kR = 0.4$, $H/R = 2.0$.)

The dependence of the drift forces on submergence, H/R, is shown in Figures 4-7 and 4-8. The experimental results are from Miyata [30]. As the body approaches the free surface the effects of wave breaking become important and the present method can not account for overturning waves. This limitation also exists with the MEL method of Cointe and the HOSM of Liu et al.

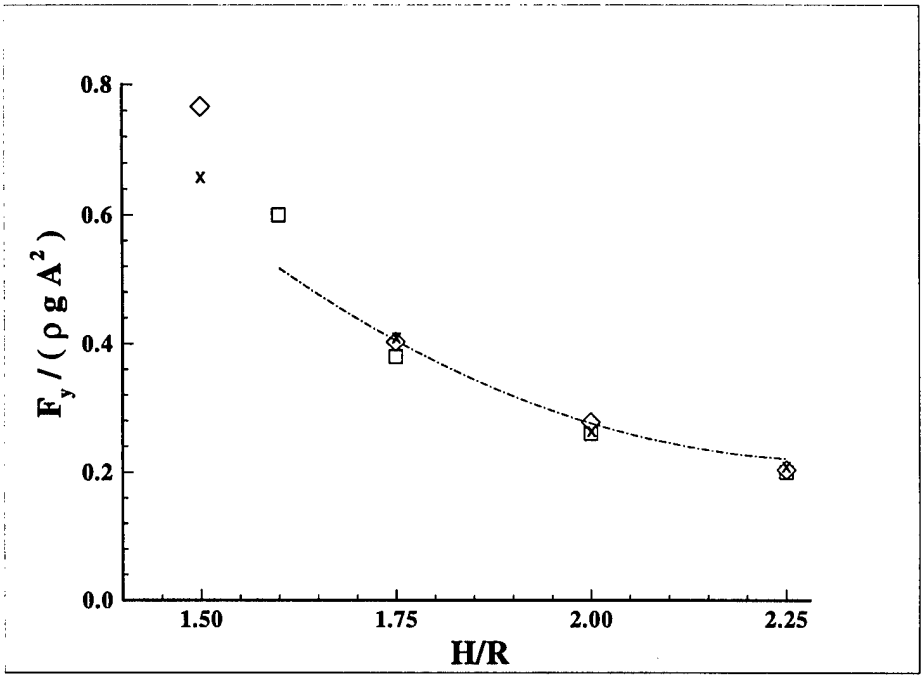

Figure 4-7: Vertical drift force as a function of submergence H/R. Experiment ($\times$); HOSM($\Box$); linear result($-\cdot-\cdot-$); present method($\Diamond$). ($kR = 0.4$, $kA = .12$ for HOSM and Experiment; $kR = 0.4$, $kA = .08$ for present method)

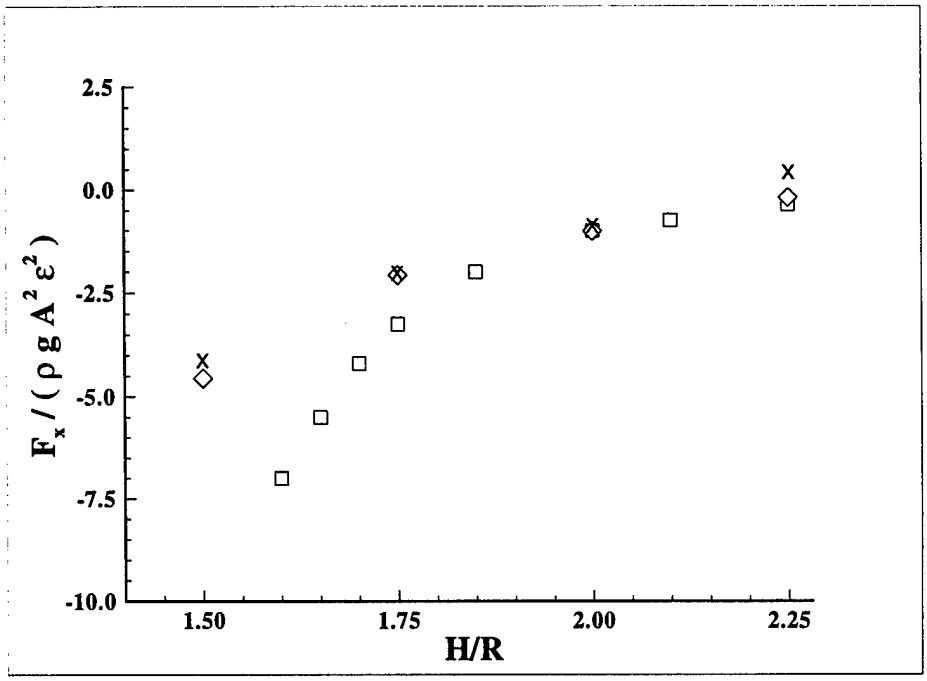

Figure 4-8: Horizontal drift force as a function of submergence H/R. Experiment ($\times$); HOSM($\Box$); present method($\Diamond$). ($kR = 0.4$, $kA = .12$ for HOSM and Experiment; $kR = 0.4$, $kA = .08$ for present method)

4.2 Diffraction by a Cylinder of Pontoon Cross Section

The ability of the combined method to compute forces on bodies of arbitrary geometry is demonstrated by computing the forces resulting from the interaction of a cylinder of pontoon cross section with incident waves. The pontoon shape is shown in Figure 4-1. The cylinder's geometric definition is the one used by Vada [48]:

$$\begin{aligned} x &= \frac{\cos\theta - \alpha\cos 3\theta}{1-\alpha} \\ y &= b\frac{\sin\theta + \alpha\sin 3\theta}{1-\alpha} \end{aligned} \tag{4.8}$$

For the shape evaluated in this thesis, $\alpha = 0.1$ and $b = 0.5$.

Method of Computing Forces

For the pontoon Equation 4.1 becomes

$$F(t) = -\rho \int_{S_B} \left[\frac{\partial \phi_T(t)}{\partial t} + \frac{1}{2}\left(\frac{\partial \phi_T(t)}{\partial s} \right)^2 \right] \mathbf{n}\, dS \tag{4.9}$$

Numerically,

$$F(t) = -\rho \sum_{i=1}^{N_B} \left[\frac{\partial \phi_{i_T}(t)}{\partial t} + \frac{1}{2}\left(\frac{\partial \phi_{i_T}(t)}{\partial s} \right)^2 \right] \mathbf{n_i}\, dS_i \tag{4.10}$$

$\partial\phi_{i_T}(t)/\partial t$ and $(\partial\phi_T(t)/\partial s)_i$ are computed by temporal and spatial central differencing, respectively.

The harmonics of the force time histories are determined using the method presented in the previous section.

Numerical Results

Time simulations of the interaction of the pontoon with waves were performed and the resultant forces compared with those of Vada[47]. The zeroeth, first, and second harmonics of the horizontal and vertical forces as functions of the body submergence, $h = H/R$, and nondimensional wave number, $K = R/(\omega^2 g)$ are presented in Figures 4-9, 4-10, and 4-11. The results for the two methods are in agreement for the range of depths and wave numbers evaluated.

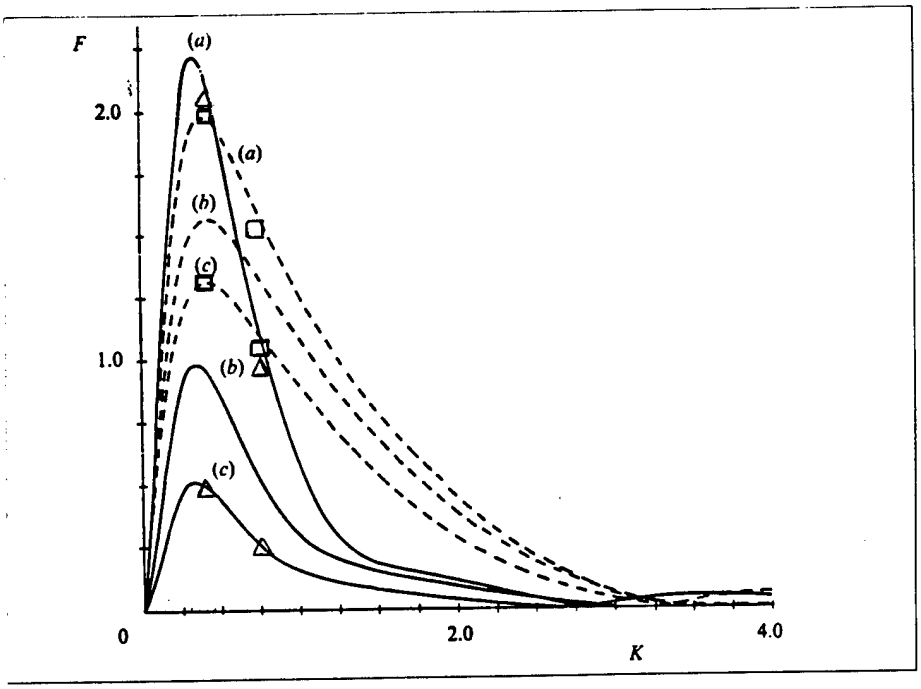

Figure 4-9: First- and second-order horizontal oscillatory forces on the pontoon. (a) $H/R = 1.0$; (b) $H/R = 1.25$; (c) $H/R = 1.5$; Vada (----, $|F_{x1}/\rho g R A|$; $-$, $|F_{x2}/\rho g A^2|$); present method ($\square$, $|F_{x1}/\rho g R A|$; $\diamond$, $|F_{x2}/\rho g A^2|$)

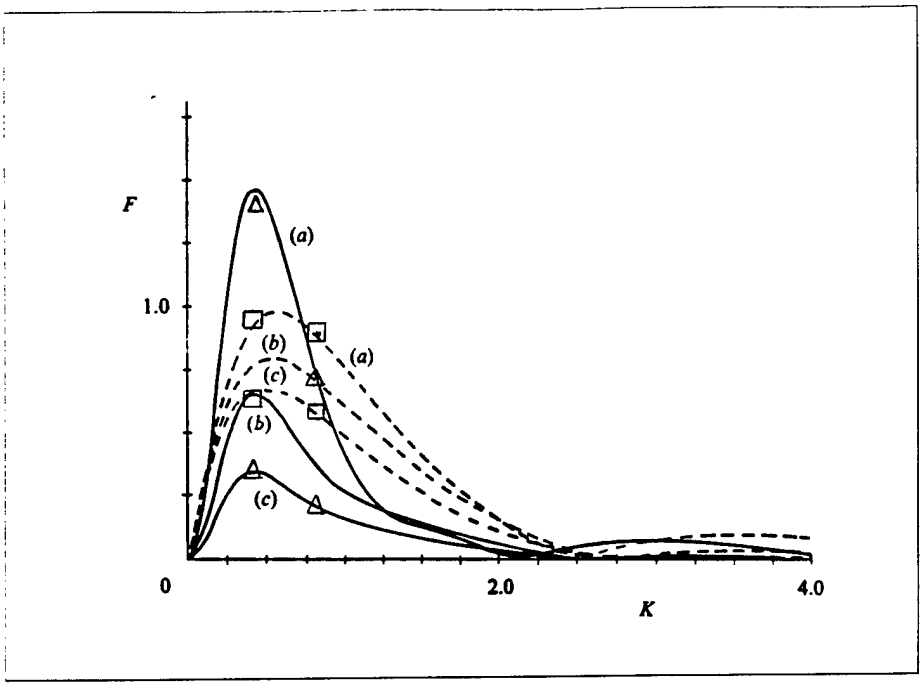

Figure 4-10: First- and second-order vertical oscillatory forces on the pontoon. (a) $H/R = 1.0$; (b) $H/R = 1.25$; (c) $H/R = 1.5$; Vada (----, $|F_{y1}/\rho gRA|$; $-$, $|F_{y2}/\rho gA^2|$); present method ($\square$, $|F_{y1}/\rho gRA|$; $\diamond$, $|F_{y2}/\rho gA^2|$)

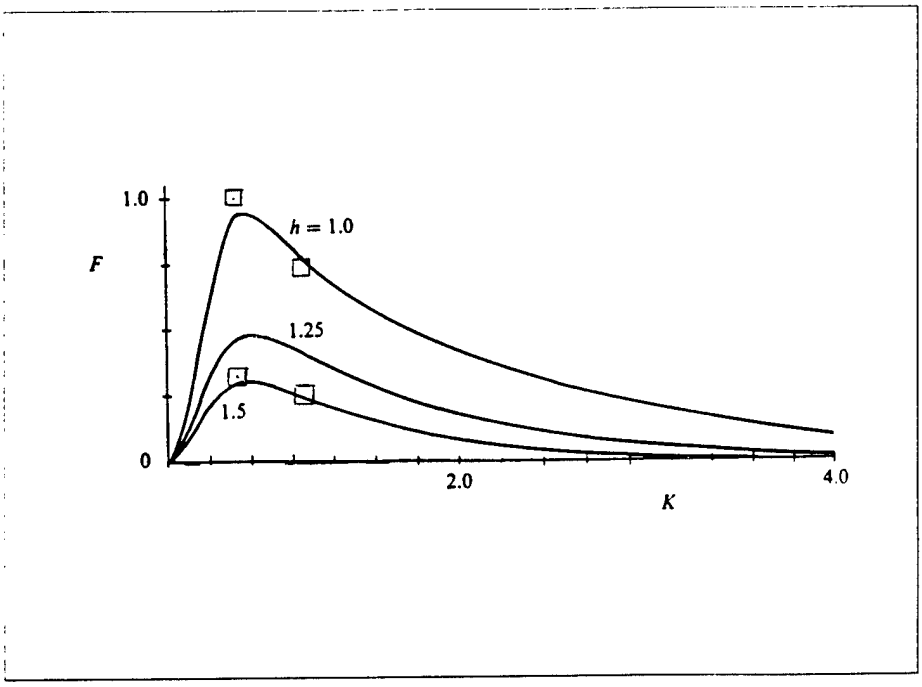

Figure 4-11: Steady vertical force on the pontoon. (a) $H/R = 1.0$; (b) $H/R = 1.25$; (c) $H/R = 1.5$; Vada $(-, |F_y/\rho g A^2|)$; present method $(\square, |F_{y1}/\rho g A^2|)$

4.3 Summary

The ability of the combined high-order spectral- boundary integral equation method to estimate the forces due to the interaction of a stationary two dimensional cylinder of arbitrary cross section with waves has been demonstrated. The method enables second order and higher forces to be computed with accuracy consistent with the accuracy of high-order spectral and Mixed Eulerian-Lagrangian methods for similar problem parameters. The present method computes free surface quantities faster than an MEL and can accommodate more general body shapes than the high-order spectral method.

In the next chapter, the combined method will be applied to the radiation problem for a fully submerged cylinder undergoing large amplitude forced oscillatory motion.

Chapter 5

Wave Radiation by a Circular Cylinder Undergoing Large Amplitude Oscillatory Motion

The purpose of this chapter is to demonstrate the application of the combined high order spectral-boundary integral equation method to the problem of a fully submerged circular cylinder undergoing large amplitude forced oscillatory motion beneath an initially quiescent free surface. Figure 5-1 defines the problem parameters.

The cylinder is forced to oscillate in heave and in circular orbital motion. The free surface profiles and the oscillatory and steady forces resulting from the forced motions are presented and compared with results generated by the other solution methods described in Chapter 1.

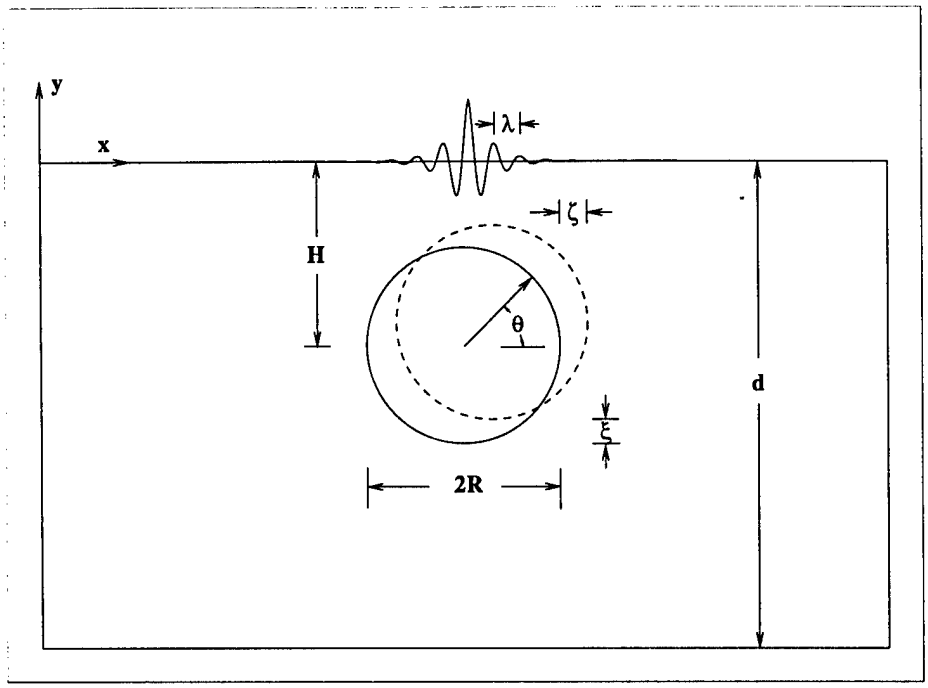

Figure 5-1: Radiation Problem Parameters

5.1 Radiation Problem for a Circular Cylinder in Heave

The forces and free surface profiles resulting from the interaction of a fully submerged cylinder forced to oscillate in heave with an initially quiescent free surface are presented in this section. The forces are evaluated as functions of:

- The nondimensional oscillation amplitude , ξ/R;
- The submergence ratio, $h = H/R$; and,
- The body radius to wavelength ratio ($\times 2\pi$), $kR = 2\pi R/\lambda$.

The forces analyzed are:

- The first and second harmonics of the vertical force; and,
- The steady vertical force.

Method of Computing Forces

The mathematical formulation developed in this thesis solves the initial boundary value problem in an earth fixed inertial reference system. For the radiation problem the expression for the force is developed from Equation 4.1:

$$F(t) = -\rho \iint_{S_B} \left[\frac{\partial \phi_T(t)}{\partial t} + \frac{1}{2} \nabla \phi_T \cdot \nabla \phi_T \right] \mathbf{n}\, dS \tag{5.1}$$

Where ϕ_T is the total potential on the body surface.

The chosen numerical formulation provides information to compute $d\phi_T/dt|_{S_B}$ directly. However, the body is moving so that $d\phi_T/dt \neq \partial\phi_T/\partial t$. The exact differential of the potential is used to develop an expression for $\partial\phi_T/\partial t$:

$$\frac{\partial \phi_T}{\partial t} = \frac{d\phi_T}{dt} - \frac{dx}{dt}\frac{\partial \phi_T}{\partial x} - \frac{dy}{dt}\frac{\partial \phi_T}{\partial y} = \frac{d\phi_T}{dt} - \vec{U} \cdot \nabla \phi_T \tag{5.2}$$

Equation (5.2) is combined with Equation (5.1) to provide the expression used for computing the force on the moving body [16]:

$$F = -\rho \iint_{S_B} \left[\frac{d\phi_T}{dt} - \frac{1}{2} \left(\nabla \phi_T \cdot \nabla \phi_T \right) + \left(\vec{U} \cdot \nabla \phi_T \right) \right] \mathbf{n}\, dS \tag{5.3}$$

In Chapter 2, two possible formulations for computing the force on a moving body, equations (2.31) and (2.32). Wu [54] performed force calculations for a surface-piercing vessel using both equations and concluded that the two equations produce different answers. The correct expression for computations involving bounded fluids is equation (2.32). Equation (2.31) is appropriate if the body is surround by a fixed control surface on which $\mathbf{U} \cdot \mathbf{n} = 0$ [33].

The time domain simulation provides the force time history in the same fashion as in the diffraction problem presented earlier in this thesis. The n^{th} harmonic coefficients of the force are computed and related to the force at each order m using the method presented in Chapter 4.

Numerical Results

The results for the radiation problem are compared with:

- The body-exact linearized free surface formulation of Wu [52] for large amplitude oscillations;
- The nonlinear BIEM of Silva and Peregrine [43];
- The linear analytic solution of Ogilvie (1963) for first order forces and the steady component of the second order force.

Trajectory

The cylinder is started from rest and the amplitude of the heave oscillation, $\xi(t)$, is increased from zero to its limit state value using the following function [26]:

$$\xi(t) = \left(1 - \exp^{-\alpha t}\right) \xi_{max} \sin(\omega t) \tag{5.4}$$

where ω is the frequency of oscillation and α is a startup constant. Equation (5.4) is used to provide a smooth startup.

Radiation Condition- Numerical Beach

The time simulations of the radiation problem are conducted until the force time history of the body reaches limit state. The method chosen to minimize the effect of transient behavior associated with the startup of the body from rest increases the time required for the problem to reach its limit state. Either a large computational domain or a method to eliminate wave reflection from the boundaries of the computational domain is required to ensure that the solution reaches its limit state.

The method developed by Dommermuth and Yue [8] and used by Liu [22] for enabling long time simulations for transient ship motions was used in this thesis. A tapering function was applied to the free surface elevation and free surface potential to smoothly truncate these quantities at the ends of the computational domain. The tapering function is shown in Figure 5-2.

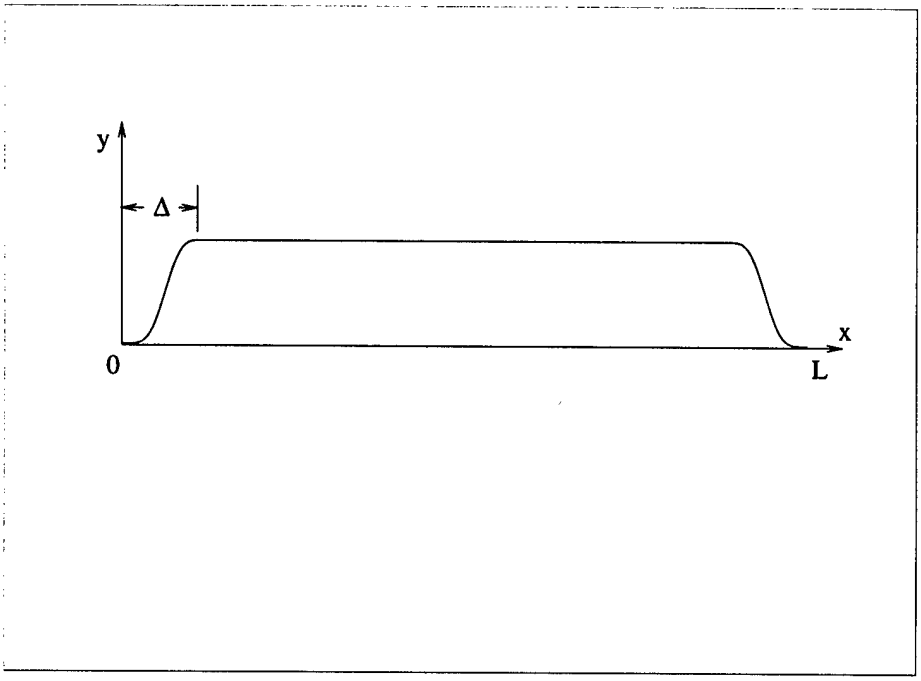

Figure 5-2: Representative tapering function.

The tapering function is defined as [22]:

$$\Omega(x,\Delta) = \begin{cases} 1, & \Delta < x < L-\Delta \\ \Pi\left((\Delta - x)/\Delta\right), & 0 \le x \le \Delta \\ \Pi\left((x - L + \Delta)/\Delta\right), & L-\Delta \le x \le L \end{cases} \tag{5.5}$$

Where $\Pi(s)$ is the Hermitian polynomial [22] :

$$\Pi(s) = 1 - 462s^6 + 1980s^7 - 3465s^8 + 3080s^9 - 1386s^{10} + 252s^{11} \quad , \quad 0 \leq s \leq 1 \qquad (5.6)$$

The width of the tapering zone, Δ, is determined by physical and computational considerations. The tapering zone must be wider than the wavelength of the longest wave generated by the oscillating cylinder. If the tapering zone is shorter than this wavelength, the wave will be too strongly "reflected" from the domain boundaries. The difference between the length of the computational domain and twice the length of the tapering zone, $L^* = L - 2\Delta$, must be long enough to allow the simulation to reach and sustain physically relevant limit state behavior. Specifically, the ratio of the wave length of the wave generated by the moving cylinder, λ to L^* must be small enough to allow multiple waves to exist within the domain. The wave length of the wave generated by the forced oscillatory motion at frequency ω is estimated by the linear dispersion relation for gravity waves in a fluid of infinite depth, $\lambda = 2\pi g/\omega^2$.

Results

The solutions for the free surface profile, the force time history, and the amplitudes of the steady and oscillatory forces generated by the combined HOSM-BIEM for the heaving circular cylinder are compared with the results generated from the other solution methods discussed in Chapter 1.

Figure 5-3 and Figure 5-4 show the free surface profile and force time history generated by Silva and Peregrine for a heaving circular cylinder. The parameters for the problem were (refer to Figure 5-1) :

- $R = 0.25$;
- $H = -0.5$;
- $d = 1.0$;
- $\xi = 0.1$; and,
- Frequency of oscillation, $\omega = 3.13$ rad/sec.

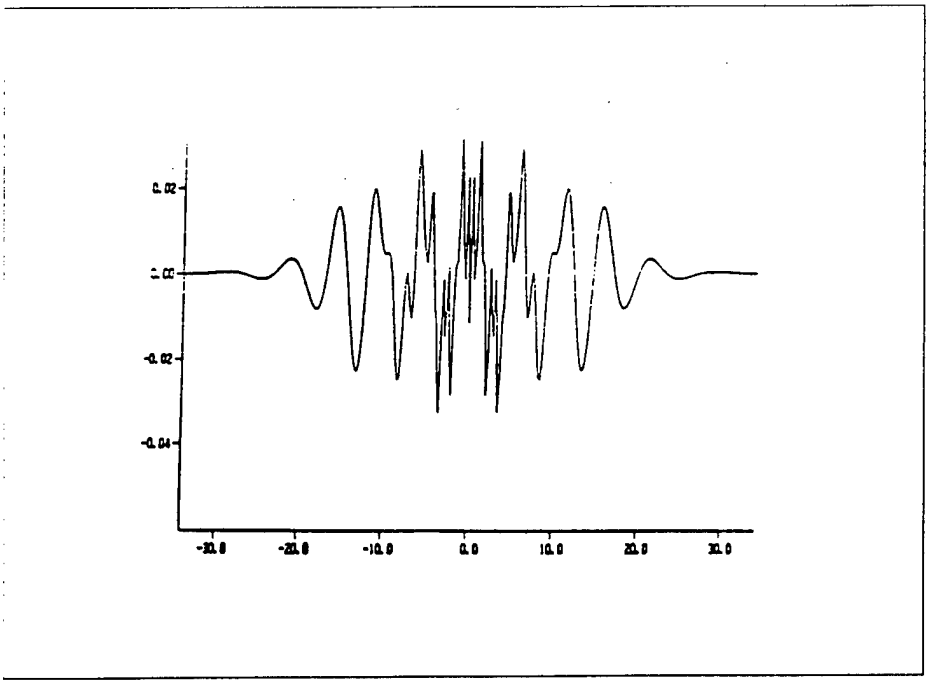

Figure 5-3: Free surface profile above heaving cylinder after approximately 5 periods of oscillation. The ordinate is the free surface elevation magnified by a factor of 500. The mean position of the cylinder center is $(0.0, -0.5)$. (Silva and Peregrine, "Engineering Analysis with Boundary Elements", 1990, Vol. 7, No. 4).

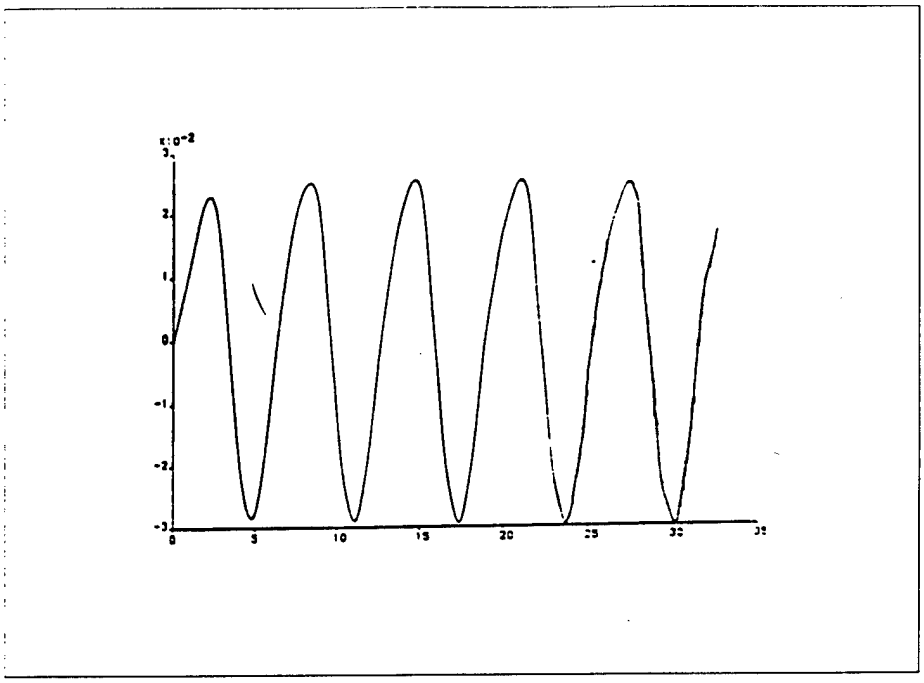

Figure 5-4: Time history of the vertical component of the force for the heaving cylinder. The ordinate is the normalized vertical force. The abscissa is time. (Silva and Peregrine, "Engineering Analysis with Boundary Elements", 1990, Vol. 7, No. 4).

Figure 5-5 and Figure 5-6 show the free surface profile and force time history generated by the combined HOSM-BIEM method for a heaving circular cylinder. The problem parameters were those listed on Page 83.

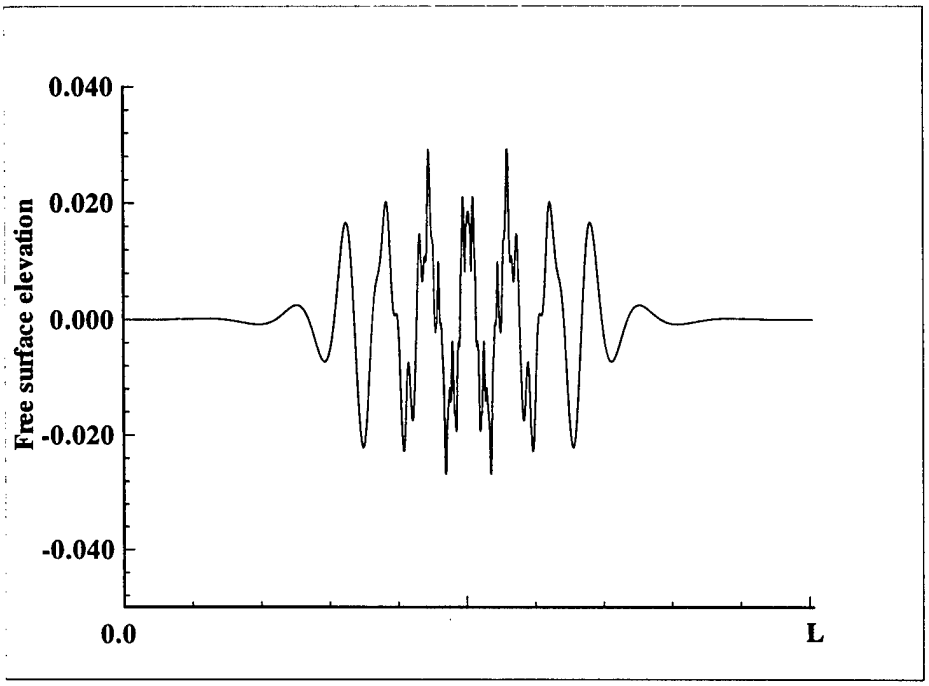

Figure 5-5: Free surface profile above heaving cylinder after approximately 5 periods of oscillation. The ordinate is the free surface elevation magnified by a factor of 500. The mean position of the cylinder center is $(L/2, -0.5)$. (Combined HOSM-BIEM method).

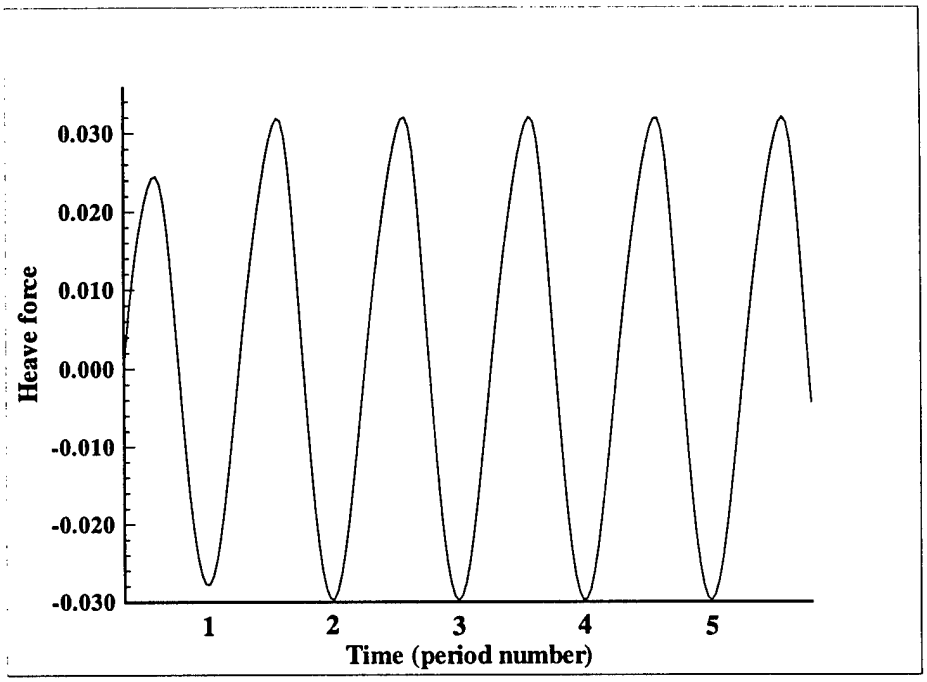

Figure 5-6: Time history of the vertical component of the force for the heaving cylinder. The ordinate is the normalized vertical force amplitude. The abscissa is time. (Combined HOSM-BIEM method).

The vertical scale for the free surface profiles presented in Figure 5-3 and Figure 5-5 are magnified by a factor of 500 to facilitate the comparison of the results generated by the two different methods. The results generated by the BIEM method of Pergrine and Silva and the results generated by the present method are qualitatively similar. A harmonic analysis of the results of Peregrine and Silva was not performed. Therefore, a more detailed comparison of the results from the two methods could not be made.

A comparison of the steady and first and second harmonics of the forces generated by the solution method of Wu [52] and the present method are presented in Figures 5-7, 5-8, and 5-9. Wu satisfied the body boundary condition on the exact position of the body and used linearized free surface dynamic and kinematic boundary conditions. Wu expressed the velocity potential in terms of a multipole expansion [52]:

$$\phi_j = \sum_{m=1}^{\infty} \sum_{s=-\infty}^{\infty} A_m^s a^m \left[\frac{e^{im\theta + is\omega t}}{r^m} + f_m^s(r,\theta,t) \right] + \sum_{m=1}^{\infty} \sum_{s=-\infty}^{\infty} B_m^s a^m \left[\frac{e^{im\theta + is\omega t}}{r^m} + g_m^s(r,\theta,t) \right] \tag{5.7}$$

$e^{im\theta+is\omega t}/r^m$ is the expression for the multipole expansion for a cylinder in an infinite fluid. $f_m^s(r,\theta,t)$ and $g_m^s(r,\theta,t)$ are required to enable the potential to satisfy the free surface boundary conditions [52].

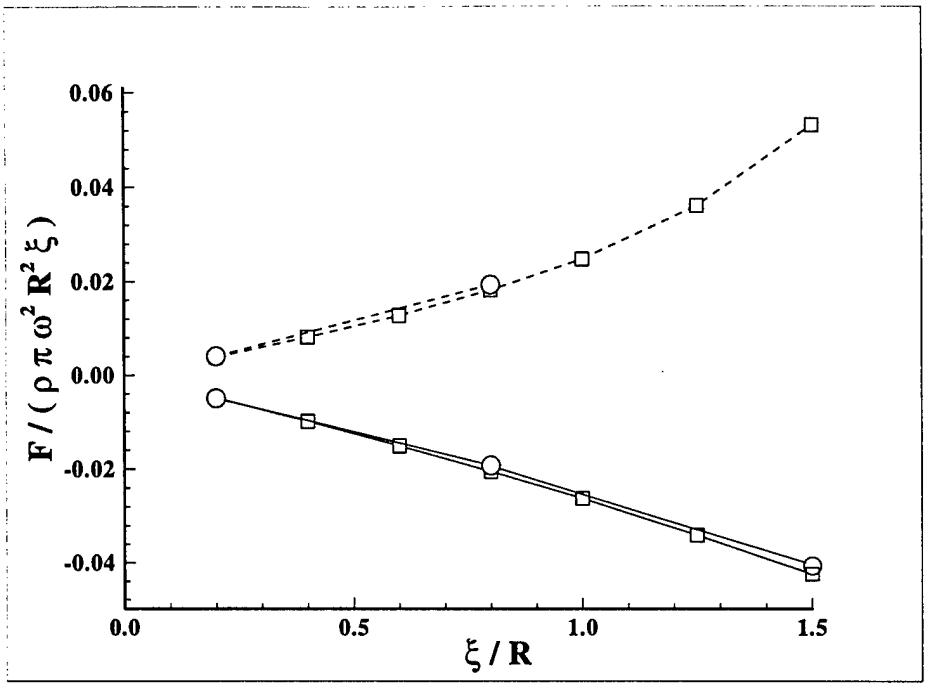

Figure 5-7: Vertical drift force on the heaving cylinder for $kR = 0.1$ (– – –) and $kR = 1.0$ (—). Wu (1993) (□) ; present method (○). ($H = 3R$).

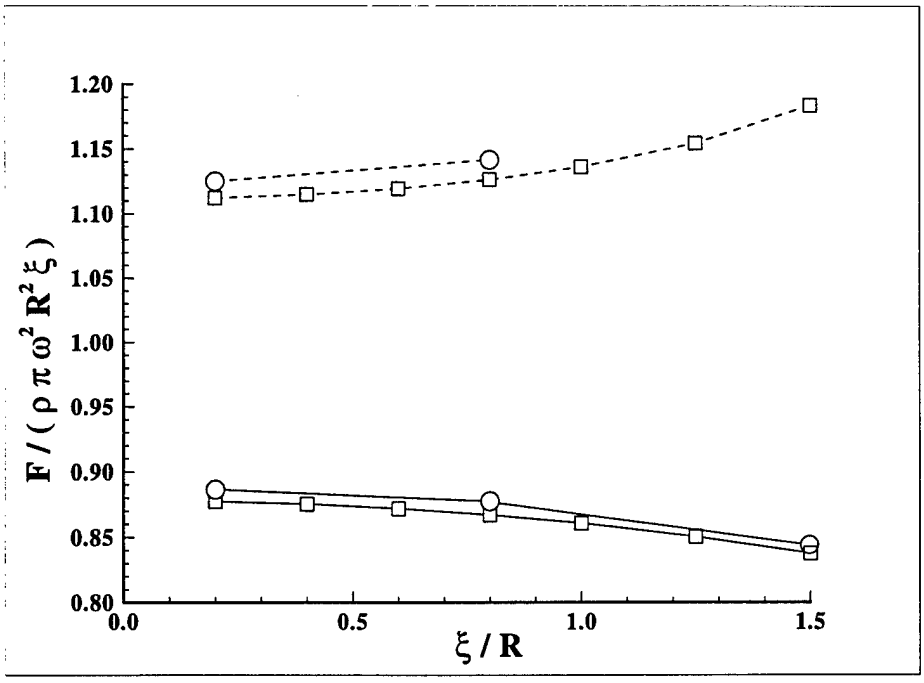

Figure 5-8: First harmonic of the vertical force on the heaving cylinder for $kR = 0.1$ (– – –) and $kR = 1.0$ (—). Wu (1993) (□) ; present method (○). ($H = 3R$).

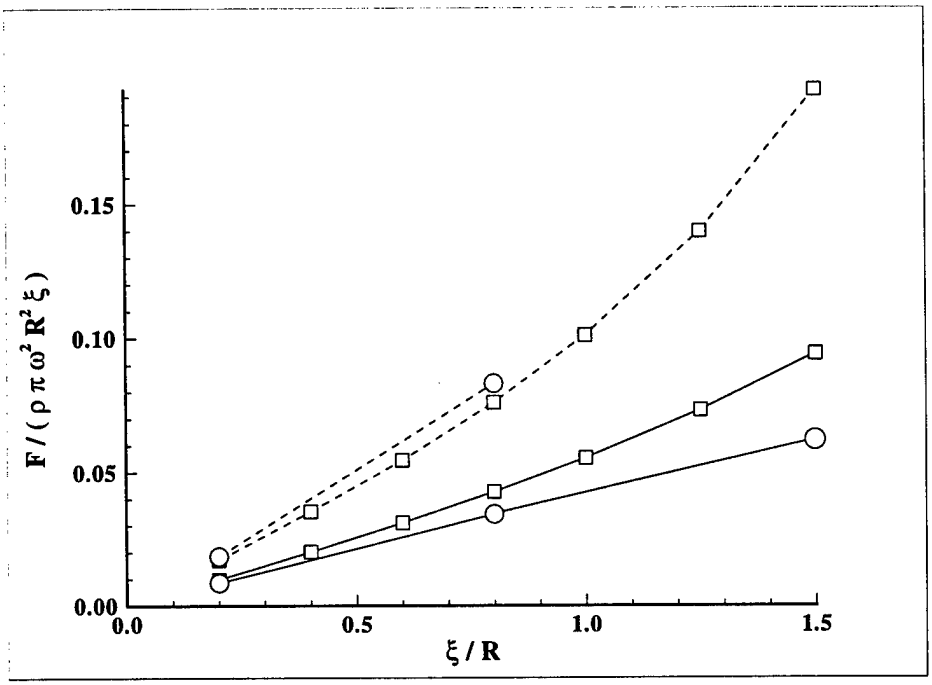

Figure 5-9: Second harmonic of the vertical force on the heaving cylinder for $kR = 0.1$ ($- - -$) and $kR = 1.0$ (—). Wu (1993) (□) ; present method (○). ($H = 3R$).

The results generated by the method of Wu and the present method agree well for heave amplitude to body radius ratios (ξ/R) less than 1.0. In the limit of vanishing heave amplitude to body radius ratios both methods converge to the linear solution of Ogilve [35].

The assumptions used by Wu to justify using the linear free surface boundary condition become invalid as the body approaches the free surface. For a deeply submerged body, the influence of the body on the free surface is of order $O(R/H)$ [52]. The linear free surface boundary condition ignores terms that involve products of order $O(R/H)^2$ [52]. For heave amplitudes greater than 1.0 the body is close enough to the free surface to invalidate the deep submergence requirement for Wu's method to be valid. In fact, for the real (physical) situation the waves break for the large orbital radii cases.

5.2 Radiation Problem for a Circular Cylinder in a Circular Orbit

The forces and free surface profiles resulting from the interaction of a fully submerged cylinder forced to undergo circular orbital motion with an initially quiescent free surface are presented in this section. The forces are evaluated as functions of:

- The nondimensional orbital radius, γ/R;
- The submergence ratio, $h = H/R$; and,
- The body radius to wavelength ratio ($\times 2\pi$), $kR = 2\pi R/\lambda$.

The forces analyzed are:

- The first and second harmonics of the vertical force, and
- The steady vertical force.

The method for computing the forces on the body and the method for starting the problem from rest are those presented in the previous sections.

Results

The free surface profile, the force time history, and the amplitudes of the steady and oscillatory forces associated with the orbiting circular cylinder are compared with the results generated from the other solution methods discussed in Chapter 1.

Figure 5-10 and Figure 5-11 show the free surface profile and force time history generated by Peregrine and Silva for the orbiting circular cylinder. The parameters for the problem were (refer to Figure 5-1) :

- $R = 0.3$;
- $H = -0.5$;
- $d = 1.0$;
- Orbital radius $= 0.025$; and,
- Frequency of oscillation, $\omega = 3.13$ rad/sec.

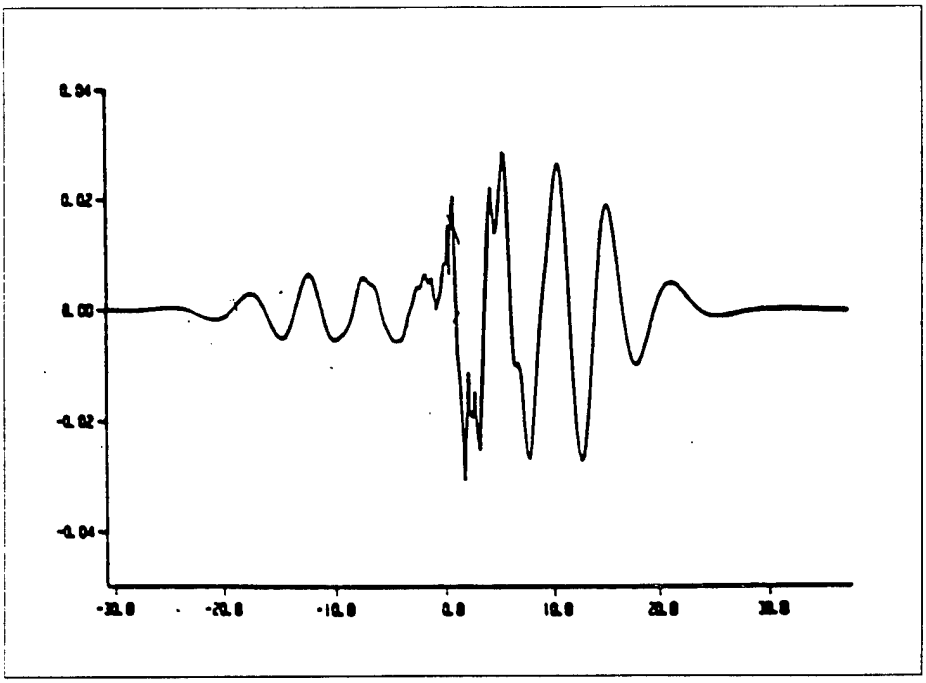

Figure 5-10: Free surface profile above the orbiting cylinder after approximately 5 periods of rotation. The ordinate is the free surface elevation magnified by a factor of 500. The cylinder center is orbiting about the point (0.0, −0.5). (Silva and Peregrine, "Engineering Analysis with Boundary Elements", 1990, Vol. 7, No. 4).

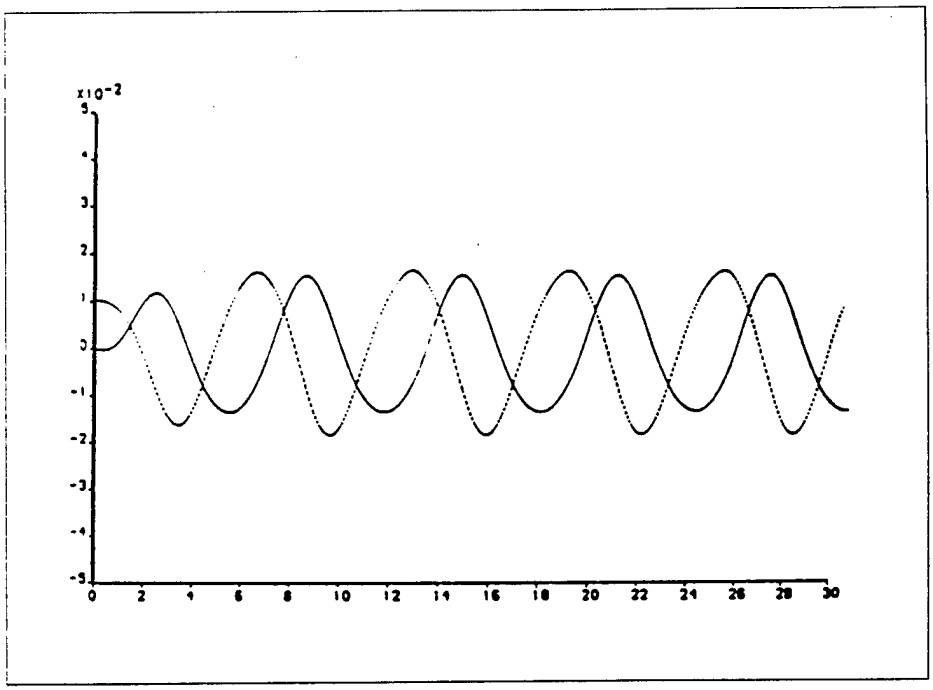

Figure 5-11: Time history of the vertical (– – –) and horizontal (—) components of the force for the orbiting cylinder. The ordinate is the normalized force amplitude. The abscissa is time. (Silva and Peregrine, "Engineering Analysis with Boundary Elements", 1990, Vol. 7, No. 4).

Figure 5-12 and Figure 5-13 show the free surface profile and force time history generated by the new combined HOSM-BIEM method for the orbiting circular cylinder. The parameters for the problem were those listed on Page 91:

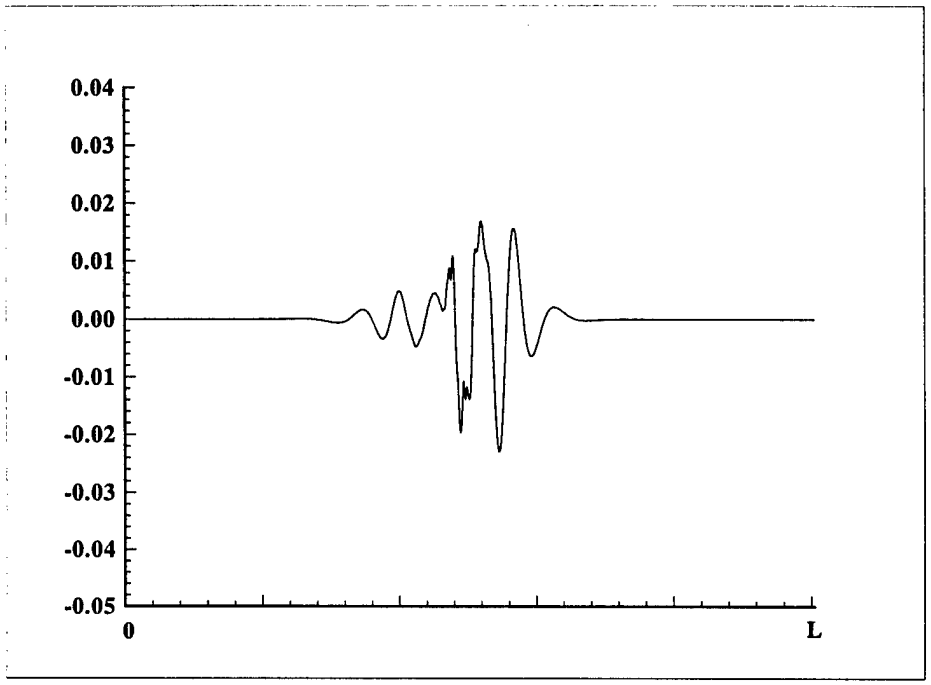

Figure 5-12: Free surface profile above the orbiting cylinder after approximately 4 periods of oscillation. The ordinate is the free surface elevation magnified by a factor of 500. The cylinder center is orbiting about the point $(L/2\ ,\ -0.5)$. (Combined HOSM-BIEM method).

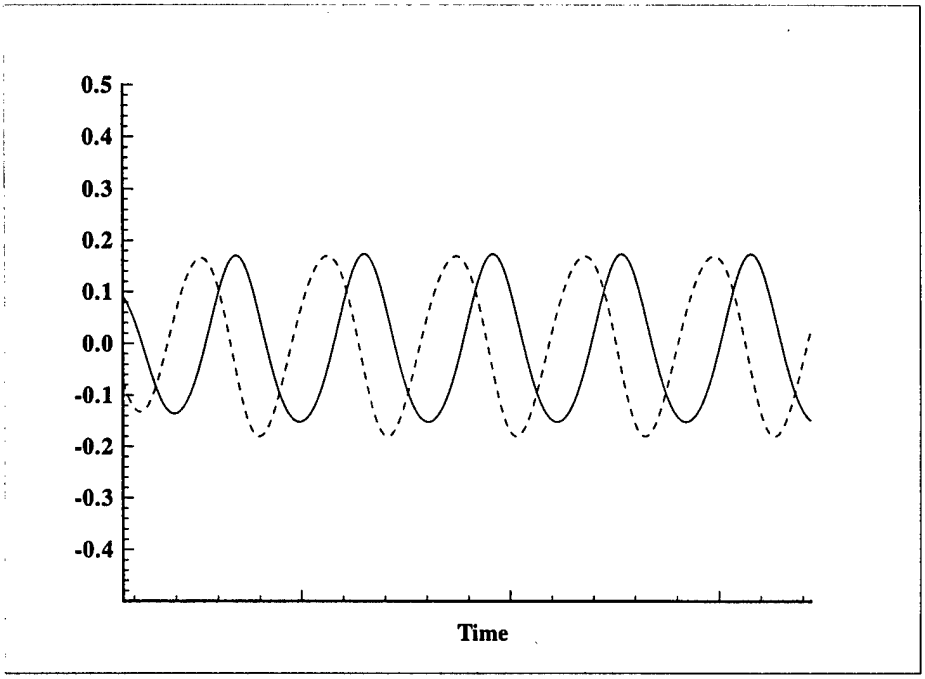

Figure 5-13: Time history of the vertical (– – –) and horizontal (—) components of the force for the orbiting cylinder. The ordinate is the normalized force amplitude. The abscissa is time. (Combined HOSM-BIEM method).

As was the case for the heaving cylinder, the comparison with the results of Peregrine and Silva provides a qualitative comparison of the results generated by these two different methods.

It has been shown that at first order (c.f. Ogilvie [35]) and at second order (Wu [53]) an orbiting circular cylinder, in a fluid of infinite extent, generates waves in one direction; e.g., a cylinder undergoing a clockwise orbit generates only right going waves. Wu [52] demonstrated that if terms up to fifth order are included in a multipole expansion representation of the potential, the possiblity of waves being transmitted in both directions exist. However, these waves are small. The results of Silva and Peregrine and the present results demonstrate that in shallow water waves of significant amplitude are generated and transmitted in the "upstream" direction.

This result is in contrast to that for a cylinder undergoing forced orbital motion in a fluid of infinite depth. Figure 5-14 shows the free surface profile above a circular cylinder orbiting beneath the free surface in a fluid of infinite depth. The problem parameters, with the exception of the fluid depth were those listed on Page 91. The cylinder generates waves in only the "downstream" direction when the fluid depth is infinite.

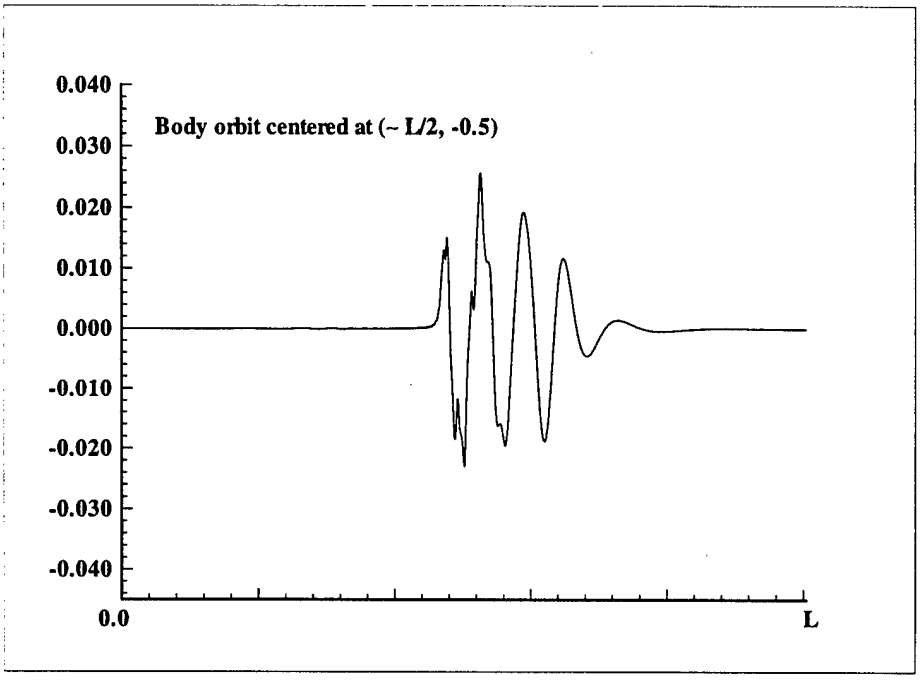

Figure 5-14: Free surface profile above orbiting cylinder in a fluid of infinite depth after approximately 5 periods of oscillation. The ordinate is the free surface elevation magnified by a factor of 500. The cylinder is orbiting about the point ($L/2$, -0.5). (Combined HOSM-BIEM method).

A comparison of the steady and first and second harmonics of the forces generated by the solution method of Wu [52] and the present method are presented in Figures 5-15, 5-16, and 5-17.

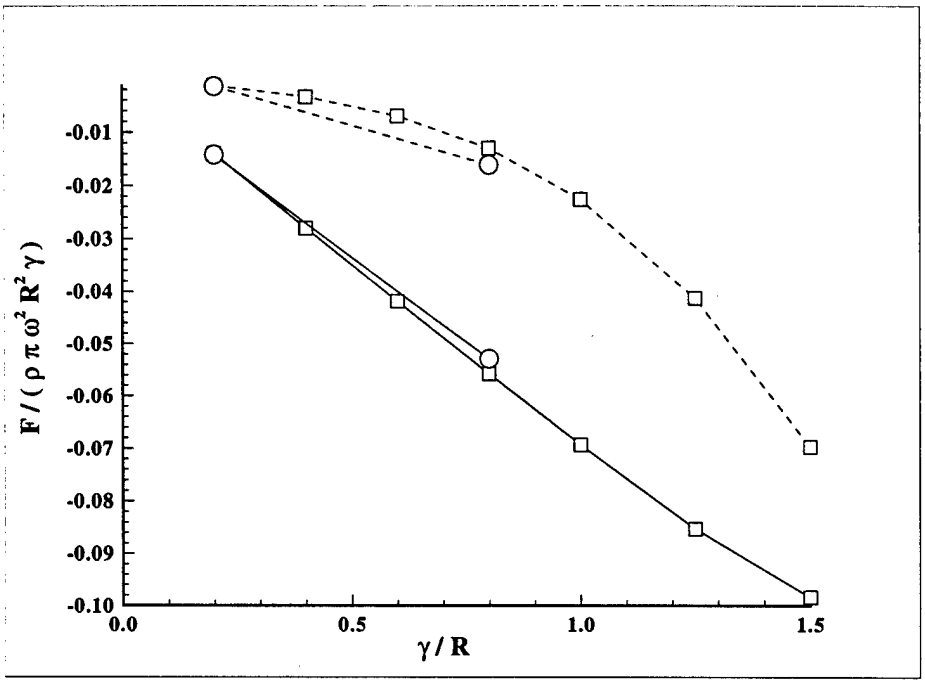

Figure 5-15: Vertical (– – –) and horizontal (—) drift forces on orbiting circular cylinder. Wu (1993) (□); present method (○). ($H = 3R$, $kR = 0.5$).

As was the case for the heaving cylinder the two methods agree well for small amplitude of oscillation (orbital radius) to cylinder radius ratios.

For large orbital radii, the cylinder generates waves with local steepnesses that exceed the limiting Stokes steepness. Figure 5-18 shows the local wave steepness for a case where the orbital radius to body radius is 1.5 and the mean depth is 3 times the body radius. For large orbital radii, the method becomes unstable as the body motion generates excessively steep waves, and does not reach limit state behavior before the simulation stops.

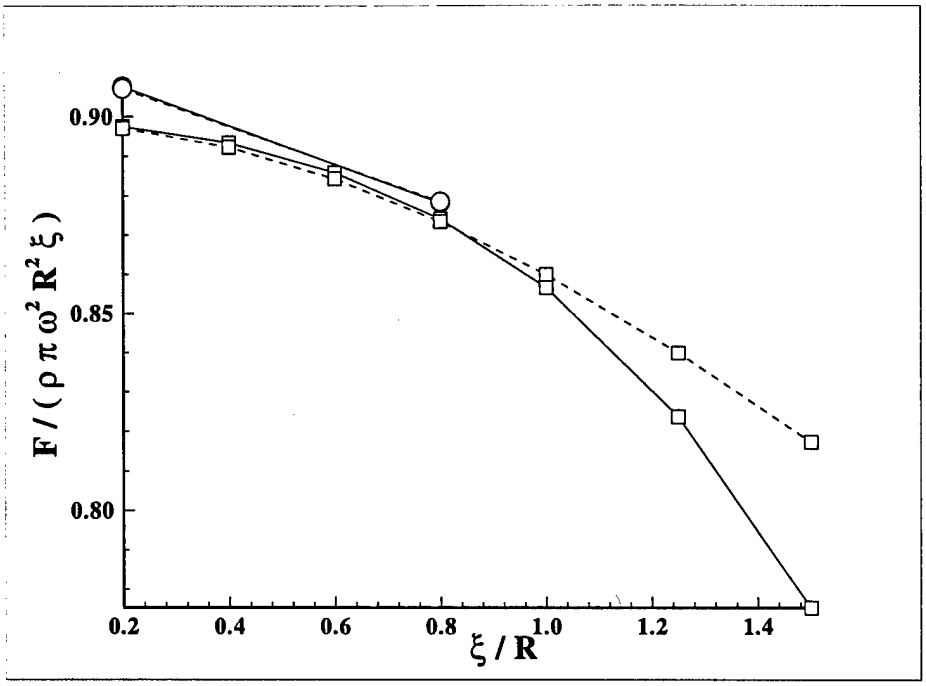

Figure 5-16: First harmonic of the vertical (– – –) and horizontal (—) forces on orbiting circular cylinder. Wu (1993) (□); present method (○). ($H = 3R$, $kR = 0.5$).

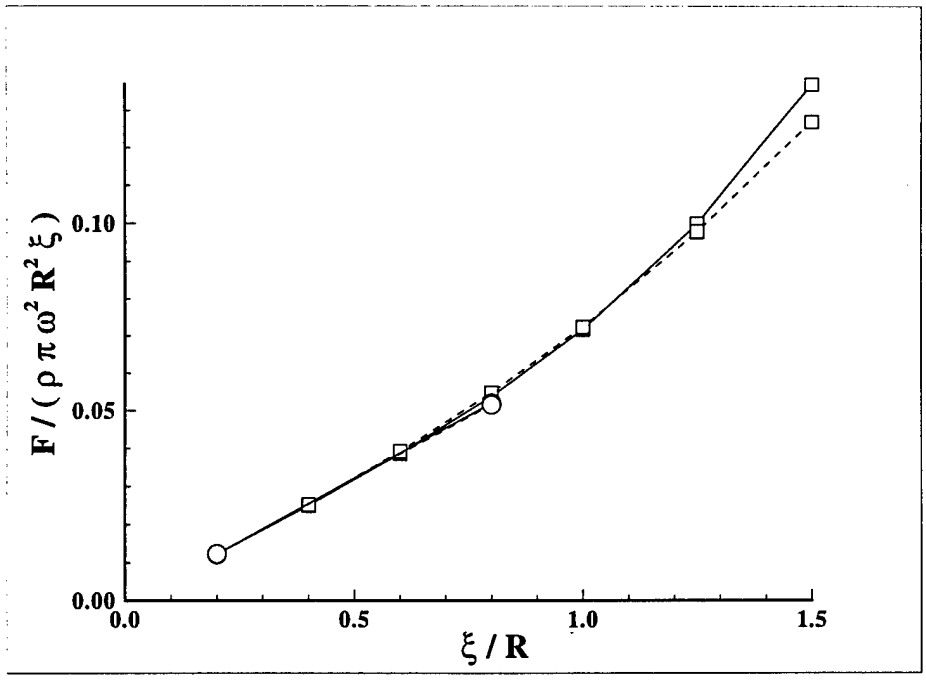

Figure 5-17: Second harmonic of the vertical (– – –) and horizontal (—) forces on orbiting circular cylinder. Wu (1993) (□); present method (○). ($H = 3R$, $kR = 0.5$).

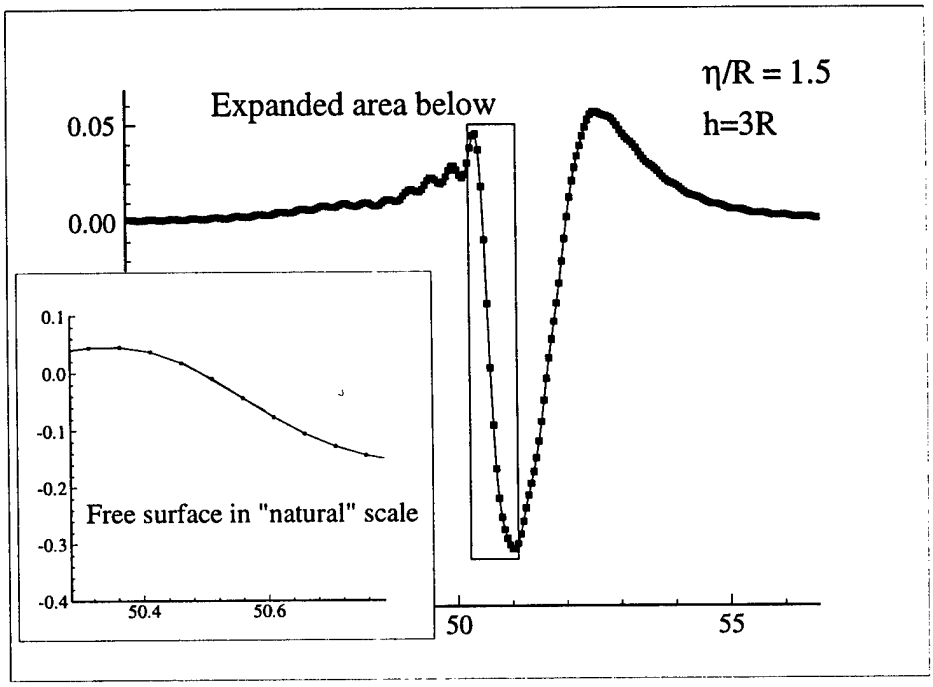

Figure 5-18: Free surface profile above the orbiting cylinder. ($H = 3R$; $kR = 0.5$).

5.3 Summary

The ability of the combined high-order spectral- boundary integral equation method to simulate large amplitude oscillatory motions of a circular cylinder beneath a free surface has been demonstrated. The method enables forces and free surface profiles to be evaluated up to limiting Stokes' wave steepness for a range of problems of interest. Problems involving either finite or infinite depth can be modelled. The importance of using a solution method which identifies the existence of physically impossible waves is demonstrated by the application of the present method to large amplitude body motions near a free surface. A method such as the one used by Wu, which does not account for non-linear free surface interactions and locally steep waves, extends linear results into flow regimes where linear assumptions are invalid.

In the next chapter, the HOSM-BIEM method will be applied to the combined radiation-diffraction problem for a fully submerged cylinder free to respond to incident waves.

Chapter 6

Combined Radiation and Diffraction Problem for a Submerged Circular Cylinder

The purpose of this chapter is to demonstrate the application of the combined high order spectral-boundary integral equation method to the problem of a fully submerged circular cylinder free to respond to an incident wave field. Figure 6-1 defines the problem parameters.

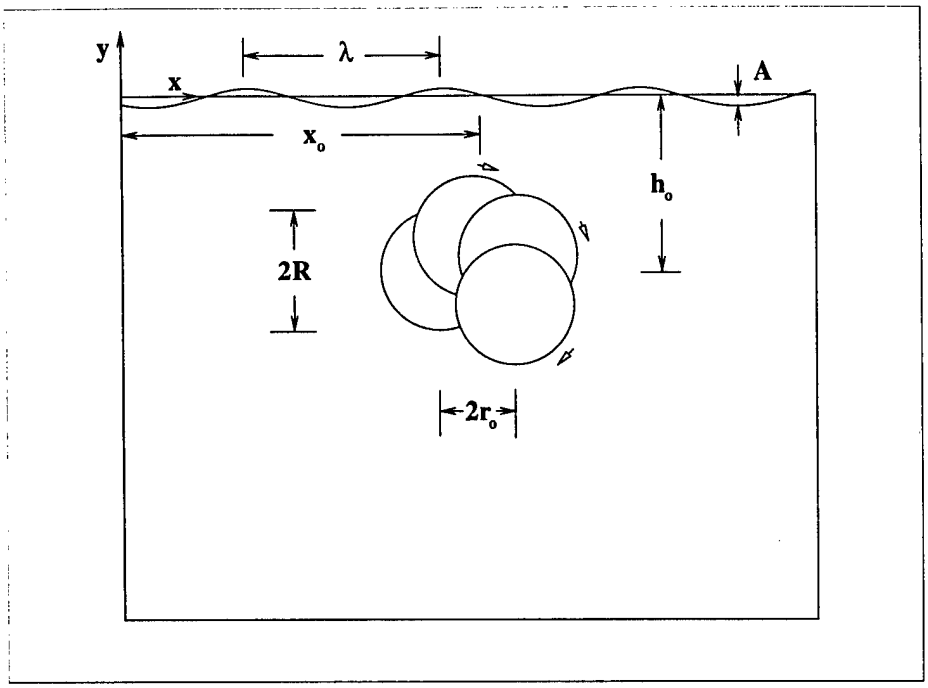

Figure 6-1: Problem parameters for the combined problem

- R = the body's radius
- r_o = the radius of body's orbital trajectory
- (x_o, h_o) = the location of the point about which the body is orbitting
- λ = the wavelength of the ambient waves
- A = the wave amplitude

6.1 The Combined Radiation and Diffraction Problem for a Circular Cylinder Free to Respond to Waves

The analyses of neutrally bouyant circular cylinders free to respond to incident wave fields were facilitated by the generation of cylinder trajectories. The cylinder trajectories were generated by:

- Specifying initial conditions for the cylinder position, velocity and acceleration;
- Solving for the instantaneous force on the cylinder using the solution methodology detailed in Chapters 2 and 3; and,
- Updating the cylinder position, velocity, and acceleration using the state varible approach represented by Equations 2.33, 2.34, 2.35, 2.36, and 2.37.

Initial Conditions

Ogilvie [35] used linear theory to show that the amplitude and phase angle of the orbital motion of a submerged circular cylinder differs from that of a water particle centered at the location of the cylinder's origin by a quantity of fourth order in kR, where k is wave number and R is the body's radius. This fact was used to estimate an intitial velocity and accleration for the cylinder.

The first-order orbital radius of a water particle located initially at (x_o, h_o) (see Figure 6-1) would be:

$$r_o(0) = Ae^{-kh_o}e^{-i\omega t}|_{t=0} = Ae^{-kh_o} \tag{6.1}$$

where ω is the wave frequency.

The initial velocity ($\vec{v_o}(t=0) = (u(0), w(0))$) and acceleration ($\vec{a_o}(t=0) = (a_x(0), a_y(0))$) of the cylinder were set the same as that of a fluid particle at the cylinder center.

$$u(0) = \omega A e^{-kh_o} \cos(kx) \tag{6.2}$$

$$w(0) = \omega A e^{-kh_o} \sin(kx) \tag{6.3}$$

$$a_x(0) = \omega^2 A e^{-kh_o} \sin(kx) \tag{6.4}$$

$$a_y(0) = -\omega^2 A e^{-kh_o} \cos(kx) \tag{6.5}$$

Method of Computing Forces and Generating the Trajectory of the Cylinder

The potential on the body is computed at each time step by solving the initial-boundary value problem presented in Chapters 2 and 3. The potential is used to compute the instantaneous force on the body, $\vec{F}(t)$, by the application of Equation 5.3. The computed force is used to update the body's acceleration, velocity, and position using the state variable representation of these quantities presented in Chapter 2:

$$\vec{a_o}(t) = \ddot{\vec{X}}(t) = \vec{F}(t)/\mathbf{M} \tag{6.6}$$

$$\vec{v_o}(t+\delta t) = \vec{v_o}(t) + \int_t^{t+\delta t} \vec{a_o}(t)\, dt \tag{6.7}$$

$$\vec{a_o}(t+\delta t) = \vec{a_o}(t) + \int_t^{t+\delta t} \vec{v_o}(t)\, dt \tag{6.8}$$

Numerical Results

The trajectories of submerged cylinders beneath waves were simulated. The waves used in the simulations were waves travelling in the positive X direction (left to right in the

figures that follow).

The convergence with respect to time step size on the trajectory of a cylinder free to respond to waves is shown in Figure 6-2. Figure 6-2 shows that in order to achieve accurate cylinder trajectories a time step size of $T/256$ or smaller is required.

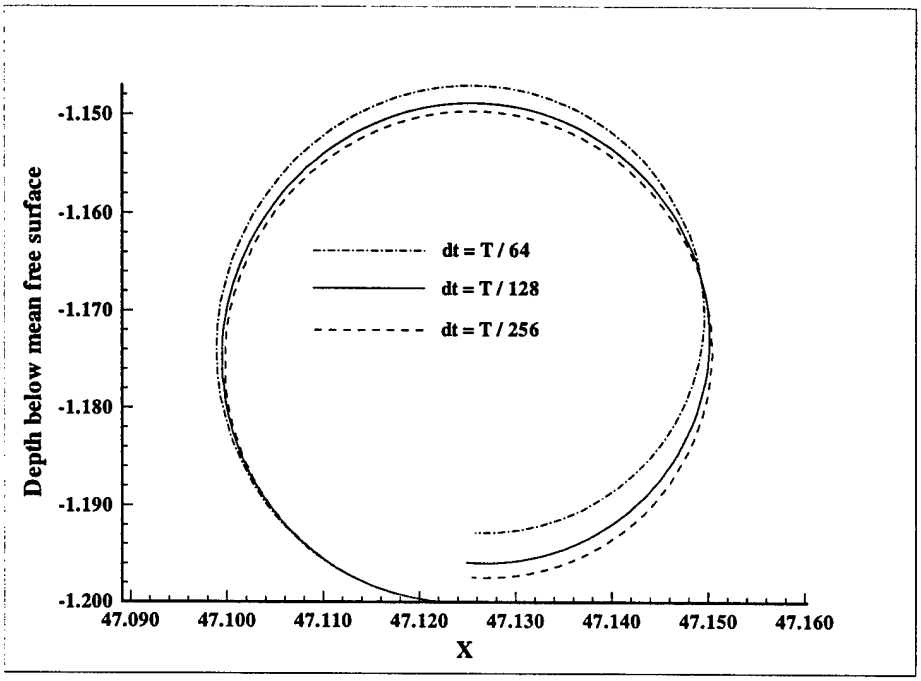

Figure 6-2: Convergence of the trajectory of a submerged circular cylinder with respect to time step size, dt. Wave slope $kA = 0.08$; cylinder initial position $(x_o, h_o) = (15\pi, -1.2)$; $kR = 0.4$. The trajectory of the cylinder center is shown. Order $M = 4$, number of Fourier modes $N_x = 2048$, domain size $N_W = 16$, $N_{filter} = 24N_W$, $N_B = 128$.

The convergence with respect to number of body segments on the trajectory of a cylinder free to respond to waves is shown in Figure 6-3.

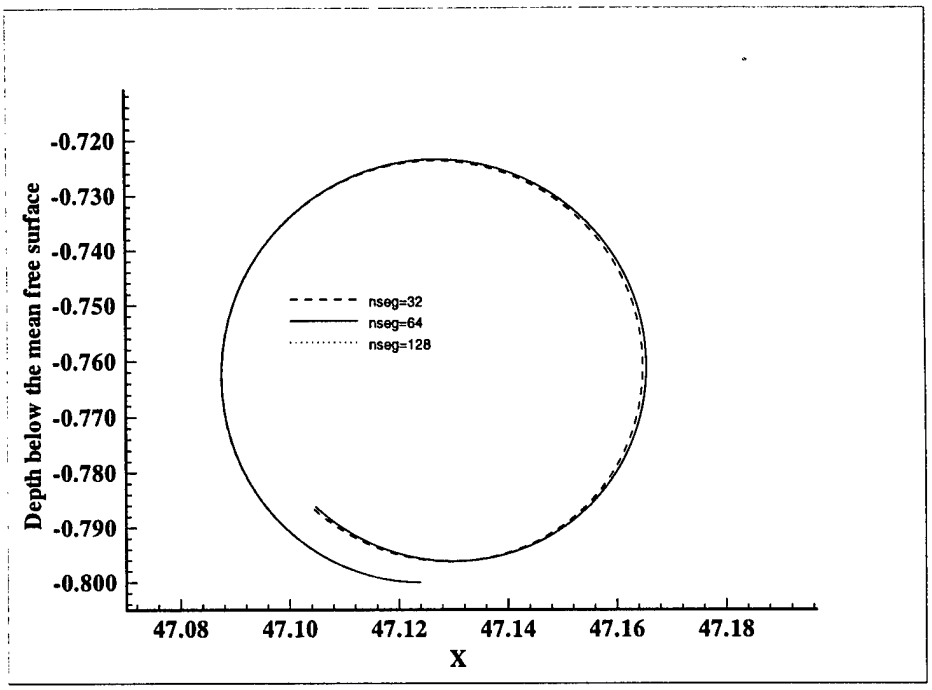

Figure 6-3: Convergence of the trajectory of a submerged circular cylinder with respect to number of body segments, N_B. Wave slope $kA = 0.08$; cylinder initial position $(x_o, h_o) = (15\pi, -1.2)$; $kR = 0.4$. The trajectory of the cylinder center is shown. Order $M = 4$, number of Fourier modes $N_x = 2048$, domain size $N_W = 16$, $N_{filter} = 24N_W$, $dt = T/256$.

Figures 6-4 and 6-6 show the trajectories for two different cylinders free to respond to incident waves. The body radius for the problem represented by Figure 6-4 is 2.5 times the body radius for the problem represented by Figure 6-6. The expanded cylnder trajectories for each case are shown in Figures 6-5 and 6-7. Figures 6-4 and 6-6 show the cylinder positions at three different time steps. The free surface profiles shown are the free surface profiles above the cylinder when the cylinders' positions are as shown by the solid lines.

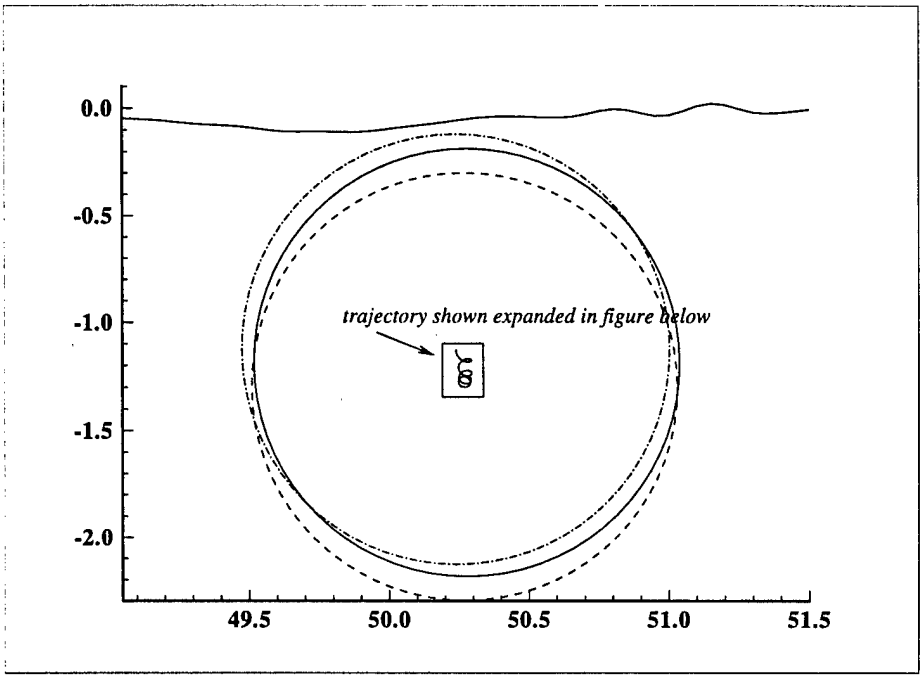

Figure 6-4: Cylinder trajectory and an associated free surface profile. Cylinder position at $t = 0$ $(- - -)$; cylinder position at $t = 3T$ $(—)$; cylinder position at $t = 3.75T$ $(- \cdot - \cdot -)$. Wave slope $kA = 0.08$; $kR = 1.0$; cylinder initial position $(x_o, h_o) = (L/2, -1.25)$. Order $M = 4$, number of Fourier modes $N_x = 2048$, domain size $N_W = 16$, $N_{filter} = 24N_W$, $dt = T/256$, $N_B = 192$.

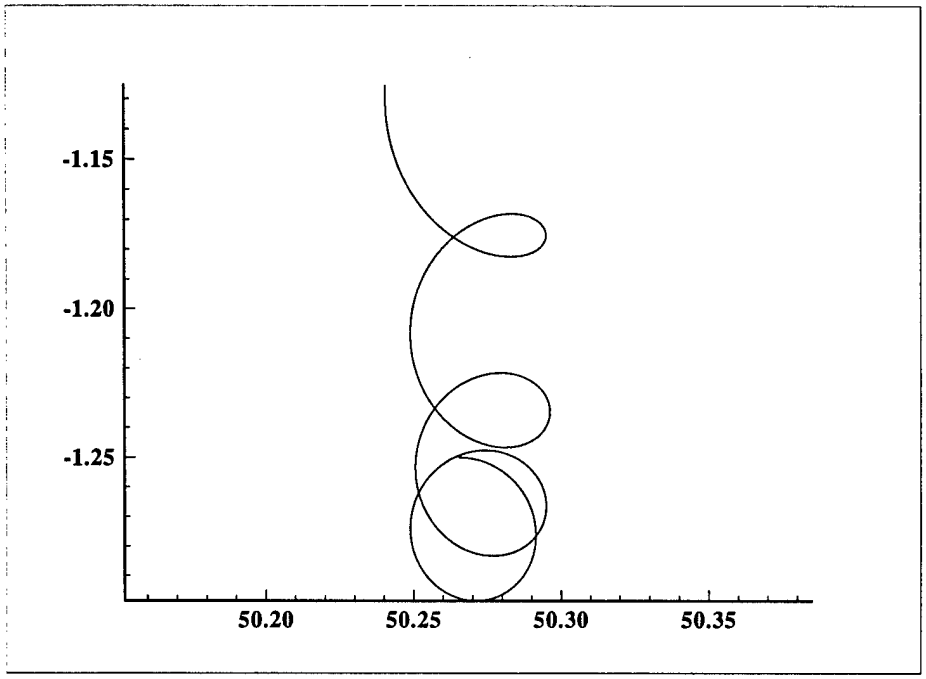

Figure 6-5: Expanded cylinder trajectory. Wave slope $kA = 0.08$; $kR = 1.0$; cylinder initial position $(x_o, h_o) = (L/2, -1.25)$. Order $M = 4$, number of Fourier modes $N_x = 2048$, domain size $N_W = 16$, $N_{filter} = 24N_W$, $dt = T/256$, $N_B = 192$.

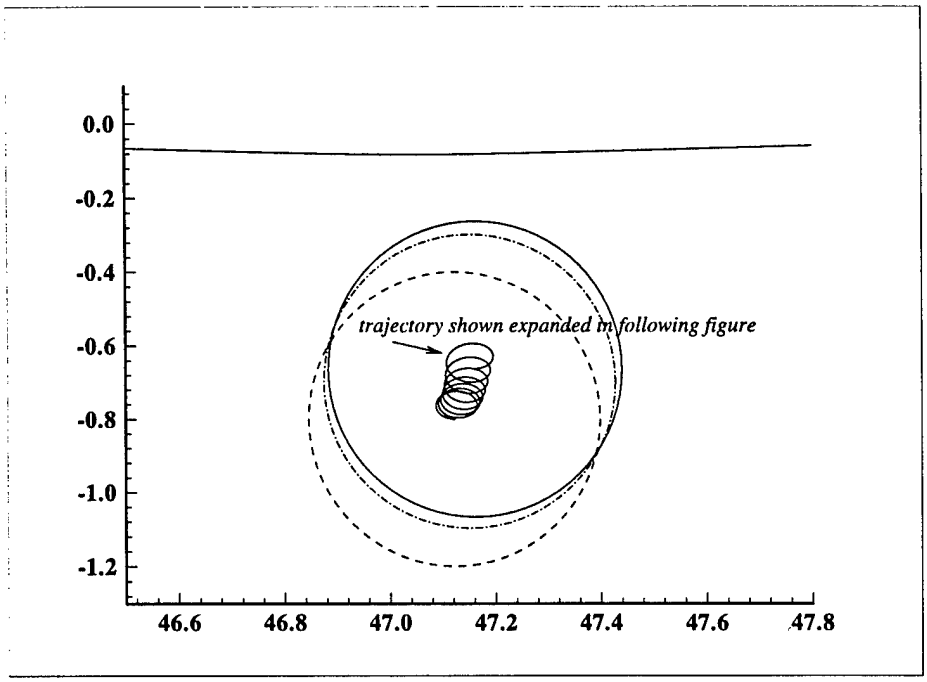

Figure 6-6: Cylinder trajectory and an associated free surface profile. Cylinder position at $t = 0$ $(- - -)$; cylinder position at $t = 3T$ $(- \cdot - - \cdot -)$; cylinder position at $t = 7T$. Wave slope $kA = 0.08$; $kR = 0.4$; cylinder initial position $(x_o, h_o) = (L/2, -1.25)$. Order $M = 4$, number of Fourier modes $N_x = 2048$, domain size $N_W = 16$, $N_{filter} = 24N_W$, $dt = T/256$, $N_B = 192$.

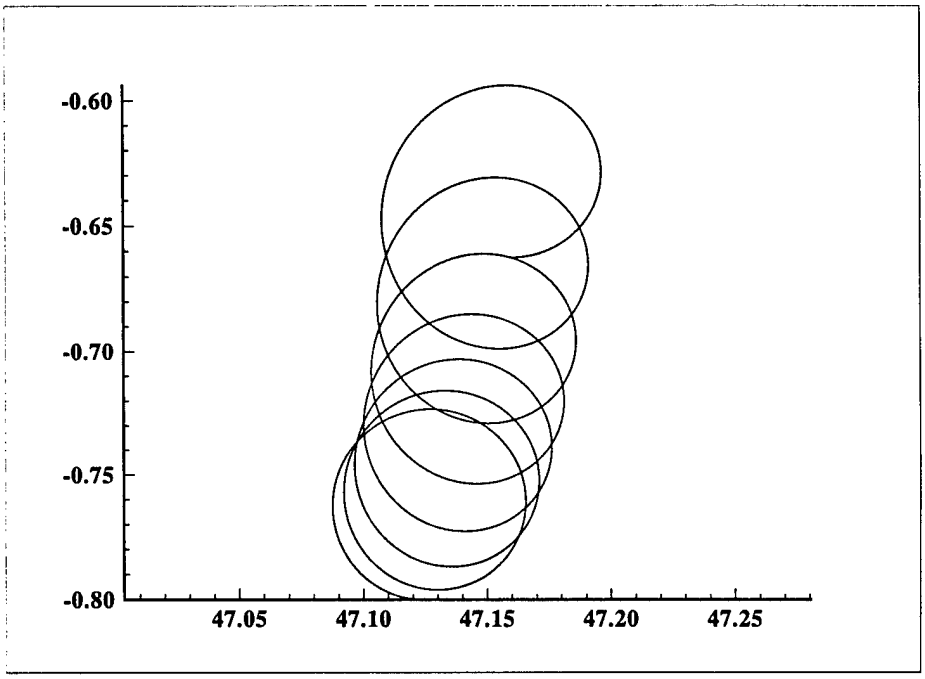

Figure 6-7: Expanded cylinder trajectory. Wave slope $kA = 0.08$; $kR = 0.4$; cylinder initial position $(x_o, h_o) = (L/2, -0.8)$. Order $M = 4$, number of Fourier modes $N_x = 2048$, domain size $N_W = 16$, $N_{filter} = 24N_W$, $dt = T/256$, $N_B = 128$.

The cylinder trajectories reflect the influence of the imposed initial conditions in that for both cases the cylinders initially follow the trajectory that would be assumed by a fluid particle located at the cylinder's initial position (x_o, y_o). As time increases the steady and oscillatory forces induced by the fluid-body interaction generate motions which differ from that of a fluid particle. For the large body the presence of a negative horizontal drift motion is apparent while for the smaller body this does not appear to be the case.

The simulation of the interaction between the large cylinder and the free surface was terminated due to the development of short, locally steep waves as the body became close to the free surface. The presence of the small locally steep waves is apparent in Figure 6-4. The development of locally steep waves helps to define the limitations of the method of this thesis and to identify flow regimes where linear theories used for modelling wave-body interactions are invalid. The free surface boundary conditions used in this thesis can not be used to simulate breaking waves.

6.2 Summary

The combined high-order spectral-boundary integral equation method has been successfully applied to the problem of a fully submerged neutrally bouyant cylinder free to respond to incident waves. The method is stable enough to enable simulations of sufficient duration to evaluate the steady and oscillatory responses of interest.

Chapter 7

Conclusions and Recommendations

A combined high-order spectral method boundary integral equation method was developed for the analysis of the nonlinear interaction of non-breaking waves with fully submerged bodies of arbitrary geometry undergoing arbitrary motions. The motivation for the development of the method was the desire to improve the computation speed for wave interaction problems involving bodies of arbitrary geometry undergoing arbitrary motions near the free surface.

The method developed in this thesis represents the total fluid potential as an expansion in a perturbation series of terms proportional to wave slope. The total potential is the sum of a spectral potential and a body potential. The method uses a spectral representation of free surface quantities and a boundary element representation of the body. The spectral representation of the free surface elevation and potential enables the fast computation of free surface quantities. The boundary element representation of the body enables bodies of arbitrary shape to be modelled. Fully nonlinear free surface boundary conditions are used as time evolution equations for the free surface elevation and free surface potential.

The effectiveness of the method was demonstrated through the study of three classes

of problems: diffraction of incident waves by a stationary body, radiation from a body undergoing forced oscillatory motion beneath a free surface, and a combined radiation-diffraction problem for a body free to respond to an incident wave field.

The success and limitations of the present method in computing the forces associated with nonlinear wave body interactions are demonstrated in Chapters 4, 5 , and 6. The present method succeeds in computing

- Oscillatory forces;
- Steady drift forces;
- Free surface profiles up to limiting wave steepness; and,
- Trajectories for bodies free to respond to waves.

The forces and free surface profiles produced by the present method for the diffraction and radiation problems compare well with those produced by other methods restricted to interactions involving non-breaking waves, and, for waves of small steepness, compare well with those produced by linear methods. Through evaluation of the free surface profiles generated by the wave-body interaction, locally steep profiles which exceed limiting wave steepness can be identified and used to determine when methods based on perturbation expansions are no longer appropriate or accurate for the characterization the posed physical problems.

The ability of the present method to evaluate bodies of arbitrary geometry was demonstrated by the evaluation of a body of pontoon cross section. The ability of the present method to evaluate bodies undergoing arbitrary oscillatory motions was demonstrated by evaluating the large amplitude oscillatory motions of a circular cylinder.

Recommendations

The present method is formulated to accomodate non-breaking waves. As shown in the analysis of the diffraction and radiation problems, locally steep waves limit the ability of the present method to evaluate wave-body interactions when the body is close to the free surface even when the waves in the ambient wave field are not steep.

The periodic nature of the formulation of the present method limits problem simulation time. For the radiation problem the use of a numerical damping zone enables longer simlu-ation times. A method for enabling long time simulations for the diffraction and combined problems needs to be developed to enable the method to perform long time simulations. This is important for the manuevering simulations where the distance travelled by a body is more than a few body lengths.

The present method was demonstrated for two dimensional non-lifting bodies. The extension of the method to three dimensions and problems involving lift is in principle straightforward, but remains to accomplished and demonstrated.

Bibliography

[1] G. R. Baker, D. I. Merion, and S. A. Orszag. Generalized vortex methods for free-surface flow problems. *Journal of Fluid Mechanics*, 123:477–501, 1982.

[2] H. B. Bingham. *Simulating Ship Motions in the Time Domain.* PhD thesis, MIT, Cambridge, MA, 1994.

[3] J. R. Chaplin. Nonlinear forces on a horizontal cylinder beneath waves. *Journal of Fluid Mechanics*, 147:449–464, 1984.

[4] R. B. Chapman. Large-amplitude transient motion of two-dimensional floating bodies. *Journal of Ship Research*, 23:20–31, 1979.

[5] J. R. Chatterton, N. K. Chhabra, A. K. Fitzgerald, and W. W. Jr. McFarland. Proximity Operations of Unmanned Undersea Vehicles. Technical Report CSDL-R-2600, The Charles Stark Draper Laboratory, Inc., 555 Technology Square, Cambridge, Massachusetts 02139-3563, May 1994.

[6] R. Cointe. Nonlinear Simulation of Transient Free Surface Flows. In 5^{th} *International Conference on Numerical Ship Hydrodynamics*, Hiroshima, Japan, 1989.

[7] D. G. Dommermuth. *Numerical Methods for Solving Nonlinear Water-Wave Problems in the Time Domain.* PhD thesis, MIT, Cambridge, MA, 1987.

[8] D.G. Dommermuth and D. K. P. Yue. A high-order spectral method for the study of nonlinear gravity waves. *Journal of Fluid Mechanics*, 184:267–288, 1987.

[9] O.M. Faltinsen. *Sea Loads on Ships and Offshore Structures.* Cambridge University Press, New York, New York, 1990.

[10] D. Gottlieb and S. A. Orszag. Numerical Analysis of Spectral Methods: Theory and Applications. In Society for Industrial and Applied Mathematics, editors, *Regional Conference Series in Applied Mathematics*, Philadelphia, Pennsylvania, 1977. J. W. Arrowsmith Ltd., Bristol, England.

[11] J. Grue and E. Palm. Reflection of surface waves by submerged bodies. *Applied Ocean Research*, 6:54–61, 1984.

[12] F. B. Hildebrand. *Advanced Calculus for Applications.* Prentice-Hall, Inc, Englewood Cliffs, New Jersey, 1976.

[13] B. Hunt. The Mathematical Basis and Numerical Principles of the Boundary Integral Method for Incompressible Potential Flow Over 3-D Aerodynamic Configurations. In B. Hunt, editor, *Numerical Methods in Applied Fluid Dynamics*, Englewood Cliffs, New Jersey, 1980. Academic Press, A Subsidiary of Harcourt Brace Jovanovich, Publishers.

[14] S. Jagannathan. Non-linear Free Surface Flows and An Application of the Orlanski Boundary Condition. *International Journal for Numerical Methods in Fluids*, 8:1051–1070, 1988.

[15] F. John. On the motion of floating bodies II. *Comm. Pure and Applied Mathematics*, 3:45–101, 1950.

[16] J. Katz and A. Plotkin. *Low Speed Aerodynamics.* McGraw-Hill, New York, 1991.

[17] J. E. Kerwin. Hydrofoils and Propellers: 13.04 Lecture Notes. 1991.

[18] B. Kinsman. *Wind Waves, Their Generation and Propagation on the Ocean Surface.* Prentice-Hall, Englewood Cliffs, New Jersey, 1965.

[19] F. T. Korsmeyer. *The First- and Second-order Transient Free-Surface Wave Radiation Problems.* PhD thesis, MIT, Cambridge, MA, 1988.

[20] D. C. Kring. *Time Domain Ship Motions by a Three Dimensional Rankine Panel Method.* PhD thesis, MIT, Cambridge, MA, 1994.

[21] W. M. Lin, Newman J. N., and D. K. P. Yue. Nonlinear forced motions of floating bodies. In *15^{th} Symposium on Naval Hydrodynamics*, Hamburg, Germany, 1984. The Office of Naval Research.

[22] Yuming Liu. *Nonlinear Wave Interactions with Submerged Obstacles With or Without Current.* PhD thesis, MIT, Cambridge, MA, 1994.

[23] Yuming Liu, D.G. Dommermuth, and D. K. P. Yue. A high-order spectral method for nonlinear wave-body interactions. *Journal of Fluid Mechanics*, 245:115–136, 1992.

[24] M. S. Longuet-Higgins. Steady currents induced by oscillations round islands. *Journal of Fluid Mechanics*, 42:701–720, 1970.

[25] M. S. Longuet-Higgins and E. D. Cokelet. The deformation of steep surface waves on water, I. a numerical method of computation. *Proceedings of the Royal Society of London, Series A*, 350:1–26, 1976.

[26] A. R. Magee. *Large-Amplitude Ship Motions in the Time Domain.* PhD thesis, The University of Michigan, Ann Arbor, MI, 1991.

[27] H. McDonald and D. Whifield. Self-Propelled Maneuvering Underwater Vehicles. In *21st Symposium on Naval Hydrodynamics*, Trondheim, Norway, 1996.

[28] D. M. Milder. A note regarding 'On Hamilton's principle for surface waves'. *Journal of Fluid Mechanics*, 83:159–161, 1977.

[29] J. H. Milgram. Note to Draper Laboratory on: Calculation of Wave Forces on Underwater Vehicles. Addresses limations in CSDL-R-2600, November 1995.

[30] H. Miyata, G. Khalil, Y. G. Lee, and Kanai. M. An experimental study of the nonlinear forces on horizontal cylinders. *Journal of the Kansai Society of Naval Architects*, 209:11–23, 1988.

[31] D. E. Nakos. *Ship Wave Patterns and Wave Patterns by a Three Dimensional Rankine Panel Method.* PhD thesis, MIT, Cambridge, MA, 1990.

[32] J. N. Newman. The exciting forces on fixed bodies in waves. *Journal of Ship Research*, 6:10–17, 1962.

[33] J. N. Newman. *Marine Hydrodynamics.* The MIT Press, Cambridge, Massachusetts, and London, England, 1977.

[34] J. N. Newman. The Green function for potential flow in a rectangular channel. *Journal of Engineering Mathematics*, 26:51–59, 1992.

[35] T. F. Ogilve. First and second-order forces on a cylinder submerged under a free surface. *Journal of Fluid Mechanics*, 16:451–472, 1963.

[36] T. F. Ogilvie. Singular perturbation problems in ship hydrodynamics. *Advances in Applied Mechanics*, 17:91–186, 1977.

[37] H. S. Olmez. *Numerical Evaluation of Nonlinear Energy Transfer to Short Gravity Waves in the Presence of Long Waves.* PhD thesis, MIT, Cambridge, MA, 1991.

[38] S. A. Orszag. Numerical simulation of incompressible flows within simple boundaries: accuracy. *Journal of Fluid Mechanics*, 49:75–112, 1971.

[39] A.J. Roberts. A stable and accurate numerical method to calculate the motion of a sharp interface between fluids. *Journal of Applied Mathematics*, 31:13–35, 1983.

[40] N. Salvesen, E. O. Tuck, and O. M. Faltinsen. Ship Motions and Sea Loads. *The Society of Naval Architects and Marine Engineers Transactions*, 78:250–287, 1970.

[41] L. W. Schwartz. Computer extension and analytic continuation of Stoke's expansion for gravity waves. *Journal of Fluid Mechanics*, 62:553–578, 1974.

[42] D. Sen, J. S. Pawlowski, J. Lever, and M. J. Hinchey. Two-dimensional numerical modelling of large motions of floating bodies in waves. In *18^{th} Symposium on Naval Hydrodynamics*, Ann Arbor, Michigan, 1990. The Office of Naval Research.

[43] A. F. T. da Silva and D. H. Peregrine. Non-linear perturbations on a free surface induced by a submerged body: A boundary integral approach. *Engineering Analysis with Boundary Elements*, 7:214–222, 1990.

[44] M. St. Denis and W. J. Pierson. On the Motion of Ships in Confused Seas. *The Society of Naval Architects and Marine Engineers Transactions*, 61, 1953.

[45] P.K. Stansby and A. Slaouti. On non-linear wave interaction with cylindrical bodies: a vortex sheet approach. *Applied Ocean Research*, 6:108–115, 1984.

[46] G. Strang. *Introduction to Applied Mathematics.* Wellesley-Cambridge Press, Wellesley, Massachusetts, 1986.

[47] F. Ursell. Surface waves on deep water in the presence of a submerged circular cylinder I. *Proceedings of the Cambridge Philosophical Society*, 46:141–152, 1950.

[48] T. Vada. A numerical solution of the second-order wave-diffraction problem for a submerged cylinder of arbitrary shape. *Journal of Fluid Mechanics*, 174:23–37, 1987.

[49] T. Vinje and P. Brevig. Numerical calculations of forces from breaking waves. In *Intl. Symp. Hydro. Ocean Engineering*, Norway, 1981.

[50] J. V. Wehausen and E. V. Laitone. Surface Waves. *Handbuch der Physik*, 9:446–778, 1960.

[51] B. J. West, K. A. Brueckner, R. S. Janda, D. M. Milder, and R. L. Milton. A new numercial method for surface hydrodynamics. *Journal of Geophysical Research*, 92:11803–11824, 1987.

[52] G. X. Wu. Hydrodynamic forces on a submerged circular cylinder undergoing large-amplitude motion. *Journal of Fluid Mechanics*, 254:41–58, 1993.

[53] G. X. Wu. Second-order wave radiation by a submerged horizontal circular cylinder. *Applied Ocean Research*, 15:293–303, 1993.

[54] Hua-Yang Wu. Simulation of the hydrodynamic interaction of bodies. Master's thesis, MIT, Cambridge, MA, 1995.

[55] V. E. Zakharov. Stability of periodic waves of finite amplitude on the surface of a deep fluid. *Journal of Applied Mechanics and Technical Physics (English Translation)*, 9:190–194, 1968.